ALMA MATER STUDIORUM · UNIVERSITÀ DI BOLOGNA

Department of Physics and Astronomy
Master degree in Physics

Lithography process optimization for high efficiency thin film solar cells

Supervisor:
Prof. Daniela Cavalcoli

Co-supervisor:
Dr. Negar Naghavi

Submitted by:
Chiara Ostendi

Academic year 2023/2024

Abstract

Copper indium gallium selenide (CIGS) based solar cells present optimal efficiency amongst thin film solar cells, with the record for cadmium-free architecture reaching 23.35%. Their high stability and low production costs, along with the possibility of being deposited on large, flexible substrates, further increase the interest on them as photovoltaic technologies. Their performances are however below the ones reached by silicon-based solar cells, especially in the field of module production. Therefore, increasing their efficiency while maintaining low production costs is crucial for making CIGS solar cells more competitive in the global photovoltaic market. One aspect that can be improved is the process through which cells are separated into sub-cells at lab-scale production, a process commonly performed through scribing.

In this work, photolithography-assisted chemical etching is explored as an alternative method for sub-cell division. This technique is indeed expected to selectively remove only the buffer and top contact layers of the cells, leaving the substrate unaltered.

The effectiveness of the photolithography method in separating the sub-cells was first tested through morphological and elemental analysis of the processed devices. Opto-electronic characterization was then carried out on cells divided into sub-cells either through photolithography or by mechanical scribing, in order to compare their performances.

The separation of sub-cells through photolithography was successful: the intended layers were properly and selectively removed, while the absorber layer was preserved. Regarding the cells' performance, higher efficiencies were consistently registered in the samples processed by photolithography, with an average increase in efficiency between the two methods of 30% for standard (1.18 eV) band-gap CIGS. The efficiency improvement was found to be determined by an increase in short circuit current and fill factors of the cells divided by photolithography, which in turn are the results of increased shunt resistance and decreased series resistance obtained with this method. The selective nature of photolithography-assisted etching is therefore found to have a positive impact on the charge collection in the cells.

Photolithography is additionally tested as a technique for the creation of a pattern for the deposition of top contact grids for wider-area sub-cells. The grids were successfully fabricated and their performance was compared to the ones obtained for scribed sub-cells with evaporated contacts.

Contents

List of compounds

NH_3 ammonia

$SC(NH_2)_2$ thiourea

$ZnSO_4$ zinc sulphate

a-Si amorphous silicon

Ar argon

AZO aluminium-doped zinc oxide

BZO boron doped zinc oxide

CdS cadmium sulfide

CdTe cadmium telluride

CGI

CIGS Copper Indium Gallium Selenide

Cu Copper

DNQ diazonaphtoquinon-sulphonate

Ga Gallium

GGI

HCl hydrochloric acid

HMDS hexamethyl disilizane

i-ZnO intrinsic zinc oxide

In Indium

ITO indium tin oxide

Mo molybdenum

Na sodium

NaF sodium fluoride

Se Selenium

SLG soda-lime glass

TCOs transparent conductive oxides

TMAH tetramethyl ammonium hydroxide

W tungsten

Zn zinc

ZnMgO zinc magnesium oxide

ZnOS zinc oxysulphide

Zr zirconium

Other acronyms

J_{sc} short-circuit current density

R_{ser} series resistance

R_{sh} shunt resistance

V_{oc} open circuit voltage

ALD atomic layer deposition

AM air-mass

BSE back-scattered electrons

CBD chemical bath deposition

EDX energy dispersive X-ray

EQE External quantum efficiency

FF fill factor

GDOES Glow-discharge optical emission spectroscopy

I-V current-voltage

OVC ordered vacancy compound

PAC photoactive compound

SE secondary electron

SEM Scanning electron microscope

STC standard test conditions

XRF X-ray fluorescence

Introduction

Photovoltaic energy is a fast growing field, key in a world where the renewable energy market is essential for contrasting climate change. In 2021 the global production of solar modules reached 190 GWp, which is a 138% increase with respect to 2016 [1], and photovoltaic now makes up 30% of the total renewable energy production. [2]

Silicon-based solar cells made up 95% of the market share and present record laboratory efficiency of 26.7% for the mono-crystalline technology. Among the possible alternatives, copper indium gallium selenide (CIGS) solar cells currently detain the record efficiency for thin-film technologies, at 23.35% for cadmium-free cells [3]. Improving the efficiency of CIGS cells while maintaining their characteristic low production cost is fundamental for the growth of this technology. One aspect of CIGS cells fabrication that can be addressed is the division of the sample in sub-cells at lab-scale production. The technique currently employed, scribing, is fast and easy, but can lead to damaging of the cells and imprecisions in the design.

On the other side photolithography is a powerful patterning technique widely used in the semiconductor industry, including photovoltaic manufacturing. Few groups [4] have reported the use of photolithography-based etching for cell division in thin film solar cells, with promising results.

This thesis work aims to the application of photolithography-assisted chemical etching on sub-cell division of CIGS solar cells, with the expectation that this technique will lead to an increase in the efficiency of the final device.

The structure of this thesis is the following.
In chapter 1 the working principle of solar cells is explained and the equations and parameters determining solar cells performances are described.

In chapter 2, the properties and structure of CIGS cells are introduced and the photolithography technique is described. Moreover the need for sub-cells separation and application of top contact grids are explained. Additionally the main techniques employed for the characterization of solar cells are outlined.

In chapter 3 the experimental process is reported. The structure of the samples is first explained, followed by a description of the steps for cell division by lithography and for front contact application. Finally, the experimental techniques and apparatuses used in this work are described.

Chapter 4 displays the results obtained during this work. A first section is dedicated to the validation of the photolithography process, both for sub-cell division and for grid application. Then the opto-electronic performances of the fabricated devices are reported and analyzed.

Finally the conclusion and future perspective of this work are reported.

Chapter 1

Background

1.1 Working principle of solar cells

A solar cell is a device capable of converting the light energy irradiated from the sun into electrical energy [5].

The sun power output as a function of the wavelength outside Earth's atmosphere is shown in figure 1.1: it presents a maximum at $\lambda = 0.5 \mu m$ and can be approximated with a black body emission spectrum at a temperature close to 5800 K.

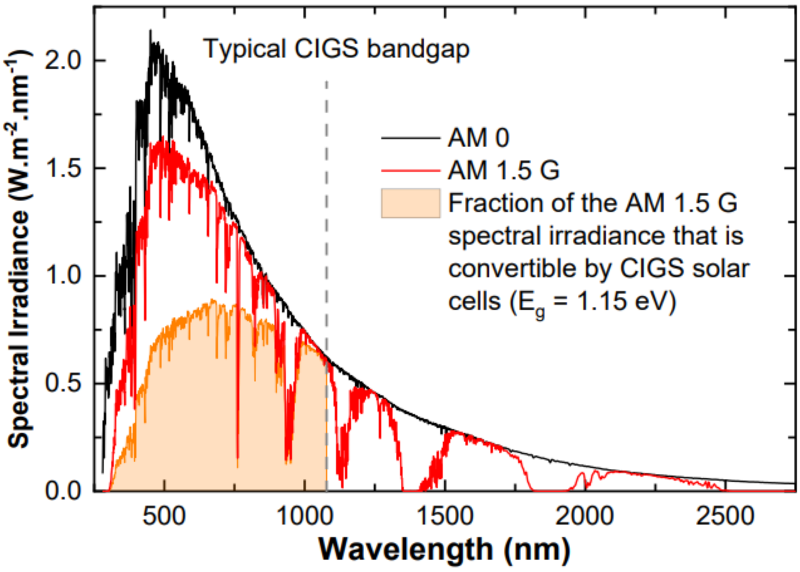

Figure 1.1: Solar spectral irradiance outside the atmosphere (AM 0) and on an average location on the earth's surface (AM 1.5 G). The shaded area represents the fraction of the solar irradiance that can be converted by a CIGS cell with 1.15 eV bad-gapn [6].

Solar radiation is however partially absorbed by gases present in the atmosphere, like water vapour, carbon dioxide, nitrous oxide or methane, and when measured on the surface will therefore show absorption lines corresponding to this compound. This absorption will depend on the path length of the light through the atmosphere and can thus be quantified by defining the air-mass (AM) coefficient, which is the ratio between the path length of light through the atmosphere and the thickness of the atmosphere it self. This coefficient will be equal to 0 outside the atmosphere, for which the *AM0* spectrum is therefore defined, and to 1 on a point on earth's surface with normal solar incidence. The global average of the air-mass coefficient is called *AM1.5G* and corresponds to an angle of incidence of 48° [7].

1.1.1 Charge generation and collection

Solar cells most commonly consist of a semiconducting p-n junction connected to a load resistance. If light with energy greater than the semiconductor's energy gap impinges on the junction, an electron-hole pair is generated. Thanks to the internal electric field generated by the junction, the charge carriers are separated before they can recombine and they are collected by electrodes placed on the two sides of the junction, generating a photocurrent.

In particular, for a cell based on a semiconductor with an energy gap E_g and an incident photon with energy $E = h\nu$, three cases are possible (see figure 1.2):

- $h\nu < E_g$: the photon cannot be absorbed by the semiconductor and therefore does not generate any charge carriers;
- $h\nu = E_g$: the photon can be absorbed and its energy is sufficient to create an electron-hole pair in the material;
- $h\nu > E_g$: the photon is absorbed and generates an electron-hole pair. However, its excess energy cannot be used by the device, and it is released through thermalization of the carriers to the band edge.

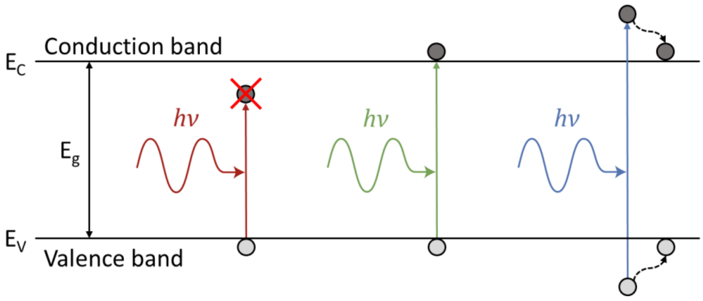

Figure 1.2: Possible interactions between a photon and a semiconductor with named gap E_g [6]

In real devices, the absorption of photons is more complex and depends on the characteristics of the material. This is quantified by the semiconductor's absorption coefficient, which is wavelength-dependent and can vary strongly between semiconductors presenting a direct band gap or an indirect band gap [6].

Moreover, not all generated carriers can be collected before recombination phenomena take place, especially if they are generated far from the depletion region where the electric field created by the junction is maximum.

The collection probability is thus dependent on the distance from the junction, as well as on the carrier's diffusion length, and in first approximation can be considered perfect for carriers generated in the depletion region or at a distance from the depletion region shorter than the diffusion length, while it decreases exponentially deeper in the bulk.

Therefore the photo-generated current density J_L can be expressed as

$$J_L \propto q \int b_S(E)\, EQE(E) dE \tag{1.1}$$

where q is the electron charge, $b_s(E)$ is the incident spectral photon flux density and the External quantum efficiency (EQE) is the probability that an incident photon will deliver one electron to the external circuit [5].

1.2 I-V characteristic of a solar cell

Since in solar cell a load resistance is present, the accumulation of separated charge carriers produces a potential difference between the terminals of the cell. This induces a current that flows in the opposite direction of the photo-generated current, leading to a reduction of the total current value. This reverse current is usually called dark current I_{dark} since it's the only component present when no external illumination is present. In dark conditions, a solar cell behaves like a diode, with a current density-voltage characteristic given by:

$$J_{dark}(V) = J_0 \left(e^{\frac{eV}{kT}} - 1 \right) \tag{1.2}$$

where e is the electron charge, k is Boltzmann constant, T is the temperature and J_0 is the saturation current.

The total current density of the cell, during illumination, is then given by

$$J(V) = J_L - J_{dark}(V) = J_L - J_0 \left(e^{\frac{eV}{kT}} - 1 \right) \tag{1.3}$$

Both the illuminated and the dark characteristics are shown in figure 1.3.

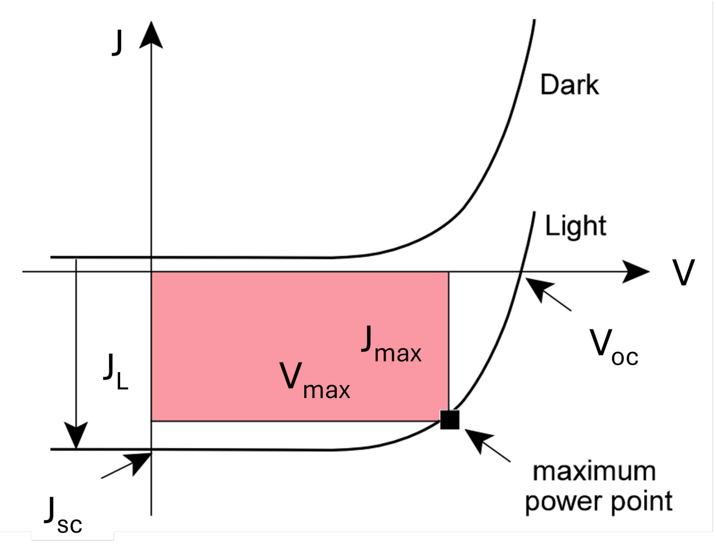

Figure 1.3: J-V characteristics of a solar cell in dark and illuminated conditions.

Solar cell parameters Three main parameters influence the performance of a solar cell: the short-circuit current density (J_{sc}), the open circuit voltage (V_{oc}), and the fill factor (FF), highlighted in figure 1.3

- **The short circuit current density** J_{sc} is the current density obtained when the terminals are connected, so for $R_{load} = 0$ and $V = 0$. It corresponds to the charge collected after generation. In this case $J_{dark}(V) = 0$ and $J(V) = J_{sc}$.
- **The open circuit voltage** V_{oc} is the voltage obtained for the cell in open voltage conditions, so for $J = 0$. In this case $J_L = J_{dark}$ and the open circuit voltage can be calculated as

$$V_{oc} = \frac{kT}{q} ln\left(\frac{J_L}{J_0} + 1\right) \tag{1.4}$$

- **The fill factor** FF determines the shape of the J-V curve and is defined as

$$FF = \frac{V_{max} J_{max}}{V_{oc} J_{sc}} \tag{1.5}$$

  where V_{max} and J_{max} are respectively the voltage and the current at the maximum power point. Their product is the maximum power output: $P_{max} = V_{max}\, I_{max}$.

The efficiency η of the solar cell is then defined as the ratio between the maximum power output P_{max} and the incident power P_{in}:

$$\eta = \frac{P_{max}}{P_{in}} = \frac{V_{max} I_{max}}{P_{in}} = \frac{J_{sc} V_{oc} FF}{P_{in}} \tag{1.6}$$

In order to accurately compare the performance of difference cells, efficiency measurements should be performed in standard test conditions (STC), so with $T = 25C$ and AMG 1.5G irradiation. [5]

In this first ideal approximation, solar cells can be modelled by a current generator in parallel with a diode, as in the equivalent circuit shown in figure 1.4.

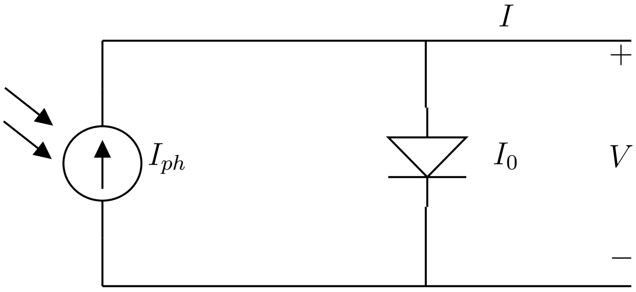

Figure 1.4: Equivalent circuit for an ideal solar cell. [8]

1.3 Efficiency limit and recombination processes

From figure 1.2 it can already be deduced that in reality it is impossible to create a cell with perfect efficiency, due to the impossibility of absorbing all incident photons and fully exploiting their energy. The limiting efficiency for a single junction solar cell in standard illumination conditions (AM 1.5 G) can be calculated in the context of the Shockley-Queisser limit [9]. Several assumptions are considered:

1. The probability of absorption of an incoming photon is unity for $h\nu \geq E_g$ and zero for $h\nu < E_g$;

2. all photogenerated carriers thermalize to the band edges;

3. in short circuit condition the collection probability of all photogenerated carriers is unity;

4. the only recombination process consists of spontaneous emission of a photon by radiative recombinations of electron-hole pairs. No other loss mechanisms, except for thermalisation and photon transparency from the previous hypothesis, are considered.

With these hypotheses, through the principle of detailed balance, it's possible to obtain an efficiency limit of $\sim 31\%$ for single junctions solar cells [10].

In real solar cells, the assumptions of the Shockley-Queisser model are hardly respected, and more loss mechanisms contribute to the reduction of the obtained efficiency [11]. In particular, different non-radiative recombination processes are present. These are mainly due to impurities creating energy levels in the absorbed band-gap, leading to processes typical of Shockley-Read-Hall recombination. These non-radiative recombination events can be implemented in the diode model of the solar cell through a non-ideality factor n, so that the J-V equation in dark conditions becomes:

$$J_{dark}(V) = J_0 \left(e^{\frac{eV}{nkT}} - 1 \right) \tag{1.7}$$

The value of the non-ideality factor depends mostly on the location of recombination sites. Recombinations in the space charge region lead to a non-ideality factor close to 2, deriving from the fact that activation energies for these processes are equal to $E_g/2$. On the other side, the non-ideality factor for recombinations in the quasi-neutral region, fr from the junction, is equal to 1. Also tunnelling recombination phenomena at the front contact can lead, to non-ideality factors greater than 1, especially in the case of thin film solar cells [9].

In order to account for all these processes, the 1-diode model for the solar cell can be expanded to include a second diode, in parallel with the first one. The two diodes will have non-ideality factors $n_1 = 1$ and $n_2 = 2$ respectively. Moreover, in real solar cells, part of the generated power is lost by dissipation through resistances at the contacts and leakage currents through the cell. These two phenomena can be addressed with the addition of a series resistance (R_{ser}) and a shunt resistance (R_{sh}), connected in parallel. The total equivalent circuit is thus the one shown in figure 1.5 and the equation describing the device becomes:

$$J(V) = J_L - J_{01} \left(exp\left(\frac{e(V + JR_{ser})}{n_1 kT} \right) - 1 \right) - J_{02} \left(exp\left(\frac{e(V + JR_{ser})}{n_2 kT} \right) - 1 \right) - \frac{V + JR_{ser}}{R_{sh}} \tag{1.8}$$

1.3.1 Multi-junction solar cells

A great part of photovoltaic research has been focused on the increase of the cells' and modules' efficiencies, and silicon technologies are now nearing the efficiency limit. In order to obtain more performative cells and overcome the Shockley-Queisser limit multi-junction solar cells have been proposed. These consist of two or more solar cells, each having a different energy gap, integrated in the same device in order to have a more efficient charge collection of the whole spectrum. Indeed, by matching cells of different gaps with photons of different wavelengths, on one side the low-energy photons can

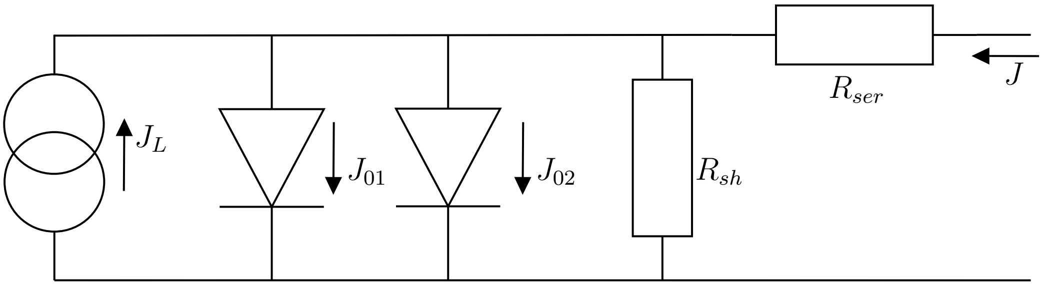

Figure 1.5: 2-diode model for real solar cells, including shunt and series resistance and accounting for different recombination modes.

be absorbed, on the other the excess energy of low-wavelength photons is not wasted in thermalization processes but is instead absorbed by materials with the same energy gap. The simplest multi-junction device consists in a stack of two cells with different energy gaps and is called a tandem solar cell, shown in figure 1.6. The top cell has a higher band gap and absorbs the highly energetic photons, while the lower energy ones are transmitted to the bottom cell, which presents a lower band-gap, in order to be absorbed [12].

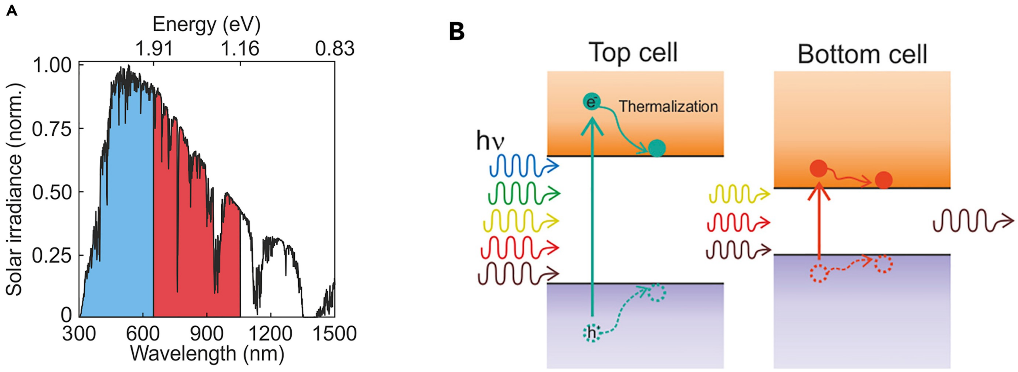

(a) Spectral response for top (blue) and bottom (red) cells in tandem configuration

.

(b) Energy diagram for tandem solar cell

Figure 1.6: Working principle of tandem solar cells [13]

Chapter 2

CIGS solar cells and their division through photolithography

2.1 CIGS cells properties and structure

Copper Indium Gallium Selenide (CIGS) solar cells are a kind of thin film solar cells whose absorber is composed of an alloy of copper, indium, gallium and selenium. They currently make up around 20% of the thin film solar cell market share, so only about 1% of global production [1]. The record efficiency reached for a CIGS single cell is 23.35%, while it is only 19.2% for a module. These values, although encouraging, are still below the ones obtained for silicon solar cells, with monocrystalline silicon reaching 26.8% for single cells and 20.4% for modules as of November 2023. [3]. However, CIGS technology is still of interest thanks to the many favourable properties it possesses.

Thanks to its direct band-gap and high absorption coefficient it is possible to obtain efficient energy conversion by using a reduced thickness of absorber, between 1-2 μm. [14]. This allows CIGS cells to benefit from the advantages of thin film technologies, like inexpensive production based on coating techniques, the possibility to deposit the absorber on flexible substrates and large area scalability. Moreover, compared to silicon solar cells, CIGS cells present a shorter energy payback time of 0.78 years for a CIGS based module, compared to 2.12 years for mono-crystalline Si cells and 1.73 years for poly-crystalline Si [15]. By employing a smaller quantity of absorber material, the CIGS cells' production process can have a reduced carbon footprint compared to wafer-based cells. Calculations based on the European PEFCR methodology lead indeed to a carbon footprint value for CIGS cell of $3.59 \cdot 10^{-2}\, kg\, CO_2\, eq/kWh$, inferior to the $4.88 \cdot 10^{-2}\, kg\, CO_2\, eq/kWh$ and $8.04 \cdot 10^{-2}\, kg\, CO_2\, eq/kWh$ values found for multi-crystalline and mono-crystalline Si respectively [16].

When compared to other thin-film technologies, cadmium telluride (CdTe) and amorphous silicon (a-Si), CIGS solar cells stand out for the higher efficiency that can be reached, since CdTe cells present single-cell record efficiencies of 21.10% while a-Si is limited at 10.2%. Moreover, CIGS has a highly tunable bandgap (see section 2.1.2), a long module lifetime of around 25 years and does not contain any toxic elements like cadmium, making it a more environmentally friendly choice. However, CIGS's share of module production is lower than CdTe, since large-scale production technologies and fabrication costs are still not competitive with this other kind of thin film cell.

In the following sections, the general structure of a CIGS-based solar cell is reported, the main properties of CIGS as an absorber are described and the principal fabrication techniques and optimization processes are outlined.

2.1.1 CIGS cells architecture

The principal architecture of CIGS solar cells in substrate configuration is shown in figure 2.1. The most common substrate is soda-lime glass (SLG), on which $\sim 1\,\mu m$ of molybdenum (Mo) is deposited, usually by sputtering. The absorber is the $Cu(In, Ga)Se_2$ alloy, which is a p-type semiconductor. The p-n junction is completed with the deposition of a thin ($\sim 30\,nm$) n-doped buffer layer. Two main materials are currently used: cadmium sulfide (CdS) and zinc oxysulphide (ZnOS), both deposited by chemical bath deposition (CBD). The top contact consists of a bi-layer stack of transparent conducting oxides, namely intrinsic zinc oxide (i-ZnO) and aluminium-doped zinc oxide (AZO) for CdS buffer layers and zinc magnesium oxide (ZnMgO) and AZO for ZnOS buffers, in both cases covering a total thickness of 400 nm. To reduce reflections an optional MgF_2 coating can be deposited over the top layer.

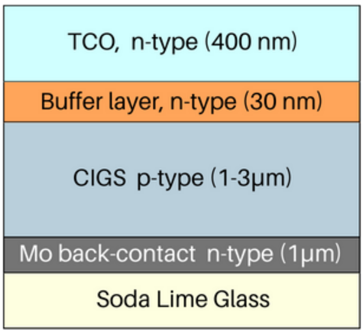

Figure 2.1: Layers composing the standard CIGS solar cells.

In the following, the main features of the different layers will be presented, based on [17] and [6], with the absorber properties described in detail in section 2.1.2.

Substrate Soda-lime glass is used as a substrate for its many favourable properties: it is transparent, inexpensive, and has a high glass transition temperature (550-600 °C), compatible with the high temperature of CIGS deposition. Its main advantage is however its high sodium (Na)content. Indeed the diffusion of Na atoms into the CIGS layers leads to an increase in the cell efficiency (see section 2.1.2). To fabricate flexible and low-cost solar cells, also polyimide foil has successfully been used as a substrate.

Back contact : Molybdenum is chosen since it is permeable to Na atoms and because it forms a thin layer of p-type $MoSe_2$ when CIGS is deposited at temperatures higher than 400°C. This interfacial layer improves the adhesion between the contact and the absorber and reduces recombination at the interface thanks to its energy gap, which is higher than the CIGS one. Moreover, the $MoSe_2$-CIGS contact is ohmic, meanwhile the Mo-CIGS contact is of Schottky type, which would cause resistive losses. Other options for back contact are transparent-conductive oxides, useful for applications in bifacial solar cells [18], or reflective back contacts, which can enhance the absorption in ultra-thin CIGS solar cells [19].

Buffer layer The buffer layer has both an electrical and a mechanical role. Indeed from one side it optimizes the band alignment throughout the cell and creates a large enough depletion region to minimize tunneling effects. On the other side, it protects the absorber from being damaged during the front contact deposition (usually done by sputtering) and prevents the formation of detrimental shunt paths. Historically, the most used buffer layer material has been CdS, which leads to consistently high conversion efficiencies of the complete cells, and which is still the standard in industry. However, this material presents two major drawbacks: the presence of cadmium, which is a highly toxic material and therefore raises environmental concerns, and its relatively low energy gap of 2.4 eV. This leads to low transparency for the cell at smaller wavelengths, resulting in a reduction of short circuit density for incident light with $\lambda < 550\,nm$. These issues led to the development of Cd-free buffer layers, the most promising of which is ZnOS. This material indeed does not contain any toxic element, can be deposited too by chemical bath deposition, and presents an energy gap tunable between 2.7-3.8 eV, which allows better photon absorption in the small wavelength range [20]. The performance of cells with Zn-based buffer layers has improved significantly in recent years, with the current record efficiency cell presenting a $Zn(O,S,Oh)_x$ buffer layer [21].

Top contact The cell's front contact must ensure simultaneously a high transparency grade to allow the incident light to reach the absorber and a high conductivity to effectively collect and transport the generated charges. For this reason transparent conductive oxides (TCOs) are mostly used. The front contact consists of two different layers: a thin, highly resistive layer and a top layer with lower resistivity. As the first layer, i-ZnO is used in the case of CdS buffer layers, meanwhile for ZnOS buffers better performances are found by employing ZnMgO, thanks to the more favourable band alignment and increased transparency [22]. Both materials can be deposited by sputtering or by atomic layer deposition (ALD), with a thickness of 50-100 nm. The other, thicker (300-400 nm) layer is instead composed of a low-resistivity material, the most common being AZO. This oxide guarantees good lateral conductivity for the free charges while maintaining the necessary transparency. Other highly conductive oxides that can be employed as front contacts are boron doped zinc oxide (BZO), which has superior transparency, or indium tin oxide (ITO) [23]. To enhance charge collection and transport on the front contact, metallic grids can be deposited on the AZO surface. More details on their role and fabrication techniques are reported in section 2.4.

In the following the buffer layer and the two top transparent oxides, so CdS/ZnOS, i-ZnO/ZnMgO and AZO for the two main configurations, will be addressed collectively as window layers.

2.1.2 Absorber properties

The absorber in CIGS solar cells is $Cu(In_xGa_{1-x})Se_2$, which is an alloy of $CuInSe_2$ and $CuGaSe_2$. These are two ternary compounds that belong to the I-III-VI semiconductors family and that crystallize in the tetragonal chalcopyrite structure. This crystal structure, shown in figure 2.2a, is derived from the zinc-blend structure of ZnSe, where the Zn sites are occupied by Cu and Ga (or In) alternatively [24].

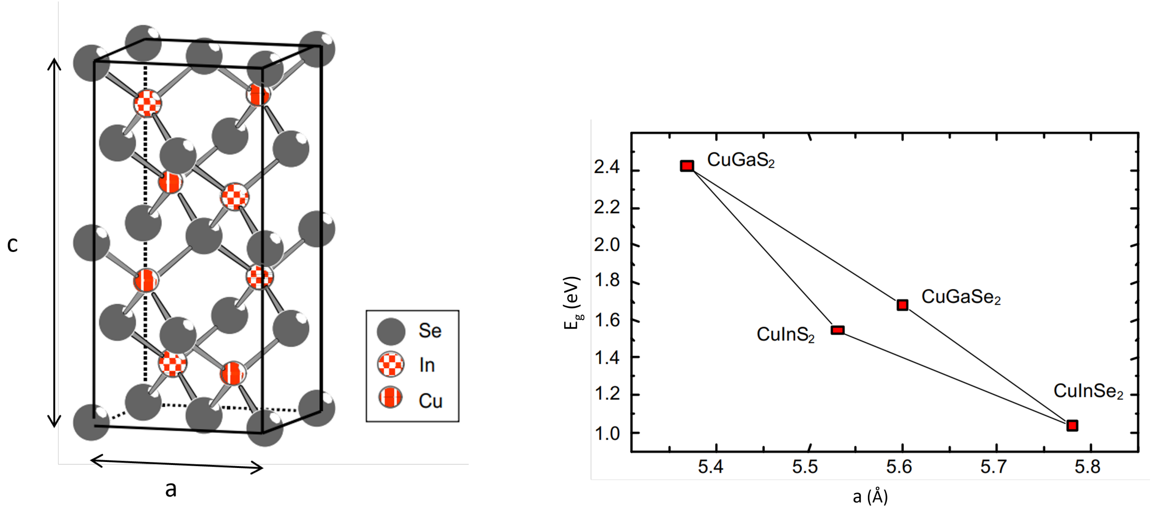

(a) Crystal structure of the CISe compound. CGSe and CIGSe molecules present the same structure, with the indium atoms totally or partially substituted by gallium atoms.

(b) Energy gap and lattice parameter a for varying $Cu(In,Ga)(Se,S)_2$ alloy compositions. In particular the values for $CuInSe_2$, $CuGaSe_2$, $CuInS_2$ and $CuGaS_2$ are highlighted.

Figure 2.2: Crystalline structure of CIGS [24].

Since the strength of the bonds between selenium and elements of group I and III are different, the structure is subjected to a distortion. This leads to a modification in the ratio c/a of lattice constants, which is no longer equal to 2. Indeed, as visible in figure 2.2b, the lattice constant a varies from $a = 5.607\,\text{Å}$ to $a = 5.780\,\text{Å}$ going from $CuGaSe_2$ to $CuInSe_2$. Analogously the lattice parameters increases from $c = 10.983\,\text{Å}$ to $c = 11.604\,\text{Å}$. [6].

Influence of gallium and copper content on the energy band diagram The composition of the CIGS alloy also influences the energy gap of the final absorber. Indeed the low energy gap of $CuInSe_2$ (1.04 eV) can be increased either by substituting In atoms with Ga atoms, since $CuGaSe_2$ has $E_g = 1.7\,eV$, or also by exchanging the selenium atoms for sulfur atoms, obtaining in the limiting cases $CuInS_2$ with energy gap of 1.73 eV or $CugaS_2$ whose energy gap reaches 2.5 eV. [17]. The values of the energy gap for these limiting cases are shown too in figure 2.2b. By varying the concentration of the elements in the $Cu(In, Ga)(Se, S)_2$ alloy is then possible to tune the energy gap within this wide range. When considering pure-selenium absorbers the energy gap is connected directly to the [Ga]/([Ga]+[In]) ratio (GGI), with the relation [25]:

$$E_g = 1.01 + 0.626 \times GGI - 0.167 \times GGI(GGI) \tag{2.1}$$

The optimal efficiencies are found at quite low energy gaps, in the 1.10-1.15 eV range, which correspond to a GGI ratio of 0.25-0.30. In particular, the current record efficiency of 23.35 % was found for $E_g = 1.08\,eV$, which corresponds to a GGI of 0.30. [21]

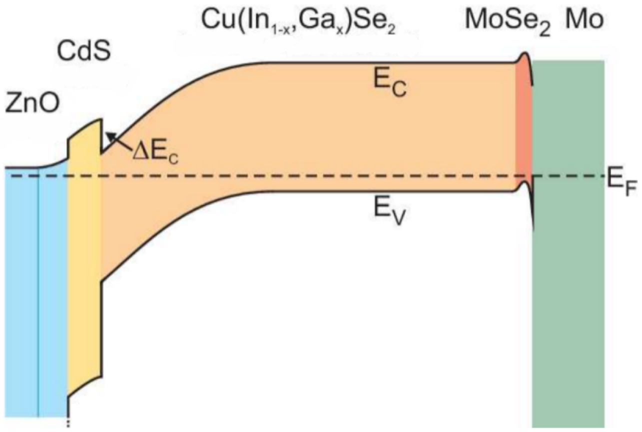

Figure 2.3: CIGS complete cell band diagram [23]

Another important concentration parameter is the (CGI), so the [Cu]/([Ga]+[In]) ratio. Indeed the best efficiencies are found for slightly Cu-deficient compositions, with GGI=0.93, which leads to the creation of ordered vacancy compound (OVC) on the top surface of the CIGS layer. This is a highly Cu-deficient thin layer, like $Cu(In,Ga)_3Se_5$ or $Cu(In,Ga)_5Se_8$, which is weakly n-type. Since the CIGS bulk is p-type (see figure 2.3), a buried p-n junction is formed at the surface, which reduces recombinations at the CIGS/buffer interface. These recombinations are additionally hindered by the higher energy gap of the OVC layer, at 1.23-1.3 eV, with respect to the CIGS, which increases the barrier for recombination.

The total energy band diagram is reported in figure 2.3, where the band alignment between the p-type CIGS and n-type top layers is clearly visible. Due to the difference in doping concentrations, the depletion region lies completely in the CIGS layer and usually presents a thickness of around 300 nm.

In order to better exploit the various influences of the different elements' concentrations, the CIGS energy band value can be graded through the layer, with the area closer to the back contact having a higher gap than the front. This is done to reduce the recombinations with the Mo contact and to favour charge separation. It is also possible to have a double-graded absorber, where the energy gap has a minimum away from the back contact and then increases again on the surface to account for the higher bandgap of the OVC layer (see Fig. 2.4).

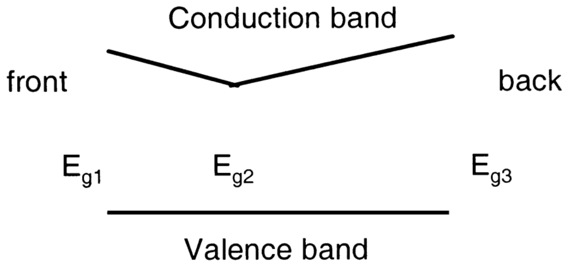

Figure 2.4: Energy gap grading at different depths of CIGS layer [6]

Effects of sodium content The behaviour of the absorber can also be influenced by the presence of impurities, in particular sodium. The inclusion of Na atom has in fact been found to result in several beneficial effects both for the morphology and the electrical properties of the CIGS layer. Its presence can lead to a smoother surface and can suppress the diffusion of Ga and In across the absorber, thus preserving the GGI grading. Additionally, it can increase the carrier concentration: Na atoms are able to substitute donor type defects that act as majority carrier traps, thus leading to an increase of hole density in CIGS and increasing p-type conductivity.

The first way to obtain Na inclusion is by diffusion from the soda lime glass substrate during CIGS deposition. Indeed, at sufficiently high temperatures, Na can migrate along the grain boundaries into the absorber creating a high enough doping concentration for the favourable effects to be present. However this process is not highly controllable or reproducible and it is restricted to only one kind of substrate and to the use of high temperatures. Therefore other methods have been developed, consisting instead of introducing Na-containing precursors or in performing sodium fluoride (NaF) post-deposition treatments. This allows controlled doping at low temperatures. [26]

Deposition techniques CIGS is mainly deposited through two techniques: co-evaporation and selenization of metallic precursors. The first method consists of the simultaneous evaporation of the elements composing CIGS in a vacuum chamber, in the presence of excess Se vapour. The deposition times, deposition temperatures and concentrations of all components can be tuned to optimize the final layer. In particular, very good results are obtained for the three-step co-evaporation method, which allows to obtain a Cu-deficient total absorber by going through a first Cu-free deposition stage, then Cu evaporation at high temperature (500-560°C) and finally another Cu-free deposition. The second fabrication technique consists instead of the deposition of the three metal precursors on the substrate, one at a time, with different possible methods like sputtering or evaporation. Then the sample is exposed to a selenium atmosphere at high temperature (around 400°C) in order for Se to react with the precursor elements and form the CIGS alloy.

CIGS in tandem solar cells The principal use of CIGS in tandem solar cells is as a bottom cell for CIGS/perovskite tandem solar cells [12]. In this case CIGS with low band-gaps are used, $\sim 1.1eV$, and a record efficiency of 27.3% have been reached [27]. Despite the great improvement registered for perovskite-based solar cells in recent years, their industrial production is however still hindered by their low stability and the presence of toxic elements in their composition.

The high tunability of CIGS band-gap would in principle allow them to be used also as the top cell of the tandem stack. A novel configuration has indeed been proposed by Barreau et al. ([28]) employing wide band-gap CIGS as the top cell and silicon as bottom cell, with a GaP buffer layer. This configuration would be based on two widely mature technologies, especially in the case of silicon, to which most industrial production is dedicated. The main limitation of this technology is the low efficiency reached by wide band-gap CIGS cells, of about 12%. Creating new strategies for increasing this value is therefore crucial for the development of these devices.

2.2 Photolithography

Photolithography is a technique through which a pattern can be transferred from a mask to the surface of a device. This is obtained by coating the surface with a light-sensitive material, called photoresist, and exposing it to UV light through the mask, presenting transparent and opaque areas. Specific chemical reactions lead to the enhancement or the reduction of the resist's solubility, resulting in only parts of the resist being preserved after the application of a developer.

The photoresist consists of three main components: the base resin, a photoactive compound (PAC) and a solvent. [29]. The base resin, like novolak in the resist employed in this work, determines the structural properties of the material, with different polymer lengths affecting the stability and the development rate. The PAC is the actual photosensitive compound. Common photoactive materials belong to the diazonaphtoquinonsulphonate (DNQ) group, which is a solubility inhibitor in the un-exposed condition. However, when exposed to UV light, the DNQ degrades: it incorporates a water molecule and forms carboxylic acid and nitrogen (see figure 2.5). This increases the solubility of the resist in alkali solutions, which can be used as developers. This process is typical of positive resists. Negative resists contain also a cross-linking agent, which is activated during light exposure. This causes the carboxylic acid to cross-link the resist during the subsequent baking stage. Therefore in negative resist the exposed areas become insoluble in the developer, while the un-exposed sections remain soluble. Negative photoresist can lead to higher resolution than positive ones.

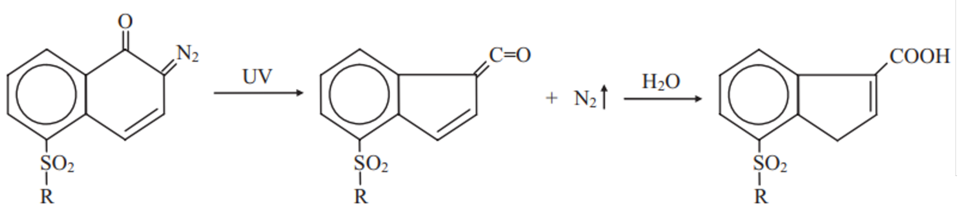

Figure 2.5: Schematic representation of the reaction occurring when DNQ is exposed to light: carboxylic acid is formed, together with the emission of N_2 and the incorporation of a water molecule [30]

The complete photolithography process comprehends multiple steps (detailed in [30] and [31]), which can be briefly explained as follows.

Substrate preparation In order to have a good, contaminant free adhesion of the resist on the surface different strategies can be implemented. The first is substrate cleaning, which can be done either a through chemical process, with subsequent immersion in solvent solutions, or by plasma or ozone etching. Additionally, in order to remove excess absorbed water the substrate is subjected to a heating process, either on a hot plate or in an oven. In this way the majority of excess water molecules are evaporated, improving adhesion and preventing unfavourable reactions with the resist. However, some water molecules can remain on the surface and react with the substrate, like in the case of silicon in which silanol molecules are formed. In this case an adhesion promoter coating is deposited on the surface, like hexamethyl disilizane (HMDS), which replaces the hydroxyl group of silanol with organic groups that enhance adhesion.

Photoresist coating The most common coating technique for photoresist is spin coating. The substrate is placed on a spin coater, which is a turntable equipped with a vacuum chuck to keep the sample in place. A small quantity of liquid resist is poured on the substrate directly with a pipette, and the surface is spun at a high speed causing the resist to spread and form a thin film. Different parameters can be tuned, like the spinning speed, the rotation time and the initial acceleration. Higher spinning speeds lead to thinner films, as visible in figure 2.6b. Different film thicknesses are employed, usually between 1-20 μm, depending on the type of resist and applications. Finally, the morphology of the final film depends also on the resist properties, like viscosity, solvent composition and volume of resist deposited, as well as the chosen substrate.

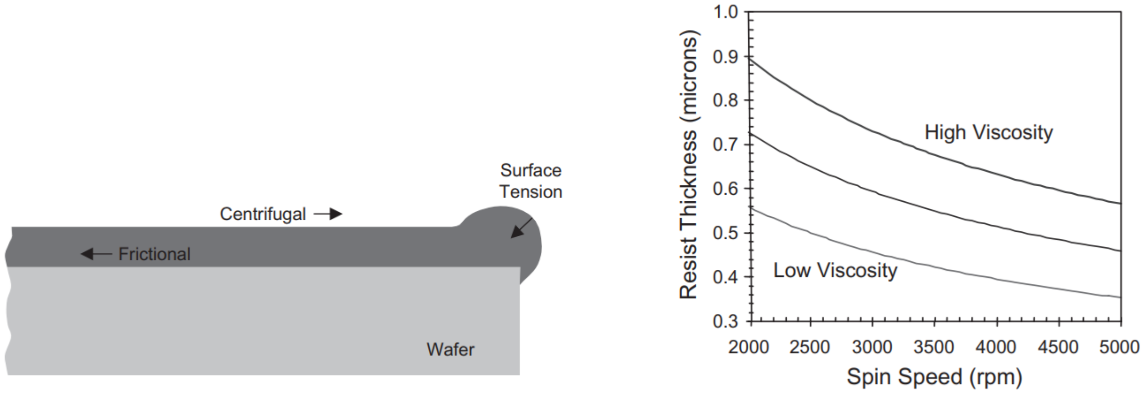

(a) Schematic representations of the forces responsible for resist distribution during spin coating

(b) Final film thickness as a function of rotation speed for resists with different viscosities

Figure 2.6: Morphology of photoresist films deposited by spin coating [30]

Spin coating is a fast and easy deposition technique. However among the most relevant downsides there are the high waste of material and the presence of edge beads, accumulations of resist at the edge of the substrates. Indeed in the initial stage of spinning, the resist is spread, thanks to centrifugal force, across the sample and the excess liquid flies off. As the film thins the centrifugal force weakens while the solvent evaporates, increasing the viscosity of the resist which in turn leads to an increase of friction. This causes a stop in the flow of the resist, which from this point on gets thinner only due to solvent evaporation, but at the same time causes an accumulation of resist at the edge, influenced by surface tension (see figure 2.6a). Especially in industrial-scale production, this difference in thickness is detrimental to subsequent processing and therefore needs to be removed.

Soft baking After spin coating the resit film still contains between 20% and 40% of solvent. This concentration needs to be decreased, in order to stabilize the film, decrease the possibility of particulate contamination, and improve adhesion. This is done by heating the sample, either in an oven or on a hot plate, in a process called soft baking or post-apply bake, until the solvent concentration reaches 3-10%. Care must however be taken to not overheat the sample. Indeed for temperatures greater than 70°C the photoactive compound starts to degrade, reducing the development rate.

After the soft-baking step, the sample needs to be cooled for a sufficient time in order to allow rehydration of the resist film. Indeed the photochemical reaction transforming DNQ in carboxylic acid requires water, which is removed from the resist during the baking step. By waiting for a certain time before exposure the water contained in the atmosphere can be absorbed by the surface of the sample. This time can vary between a few seconds for 1 μm thick resist to many hours for very thick resist ($> 30\mu m$).

Exposure Exposure to UV light (350-450 nm range) is the condition which allows the change in solubility of the photoresist. The most simple exposure configuration consists of illuminating the sample through a photomask. These are glass plates that present an evaporated metallic pattern on one side. Therefore they block the UV radiation in some zones while they are transparent in others. The most straightforward exposure mode is contact mode, in which the sample is in direct contact with the mask during illumination. With this configuration a good resolution can be obtained, $\sim 1\mu m$, but the contact can cause residues of resist to stick to the mask or even damaging it, making this setting not ideal for large-scale production. These problems can be avoided by leaving a gap between sample and mask, in 'proximity' mode. However, the resolution of the pattern scales as

$$resolution \propto \sqrt{g\,\lambda} \tag{2.2}$$

where λ is the light wavelength and g is the gap between mask and sample substrate. Therefore proximity mode results in lower resolution than contact mode.

An alternative solution is performing exposure in projection mode, in which the image of the masks is projected onto the sample surface by a lens. This method leads to both good resolution and minimal damage of the mask, but requires more advanced optical components and calibration procedures. The different exposure methods are portrayed in figure 2.7.

In all cases, a careful alignment between mask and sample is necessary, especially in devices which require multiple lithography steps for different components.

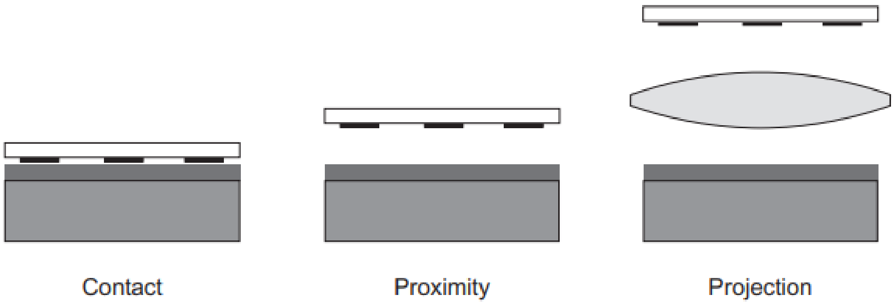

Figure 2.7: Different exposure modes: a) contact, b) proximity, c) projection [30]

Hard baking A second baking step is performed at high temperatures (100-130°C) after the exposure. In positive resist, this is mostly useful for diffusion of the photoactive compound across the resist layer. This can help in smoothening some edge ridges, caused by interference phenomena during exposure. In negative resists the post-exposure baking causes the cross-link of the exposed resist, making it insoluble in the developer. The sample should again be cooled before the development stage.

Development In the development stage the soluble sections of the resist, which were the ones exposed for positive resist and unexposed for negative resists, are dissolved by a developer. Acqueus-based developers are often used, like tetramethyl ammonium hydroxide (TMAH), but organic-based developers are also available. The sample can simply be submerged in the developer solution, but other techniques like spray development, spin development or puddle development are also used for in-line production. The development rate depends on temperature, developer dilution and type of resist.

Etching or lift-off At this stage the deposition and patterning of the photo-resist is complete and the substrate will present areas covered in stable resist and areas where the surface is exposed. The device is then processed through three main techniques: etching, lift-off or ion implantation, which is used for selectively doping only sections of the substrate.

Etching is a subtracting technique which implies the removal of a layer of material in the exposed areas, either through *wet etching* or *dry etching* techniques. Wet etching, which is used in this work, is performed through an etchant solution, usually an acid, in which the sample is submerged. This leads to an isotropic etching of the sample, since the solution erodes the material along all directions, and can results in an undercut in the etching profile. Dry etching, which is often performed by means of a plasma, is instead isotropic thanks to the directionality of the plasma.

Lift-off is an additive process through which material is selectively deposited only on

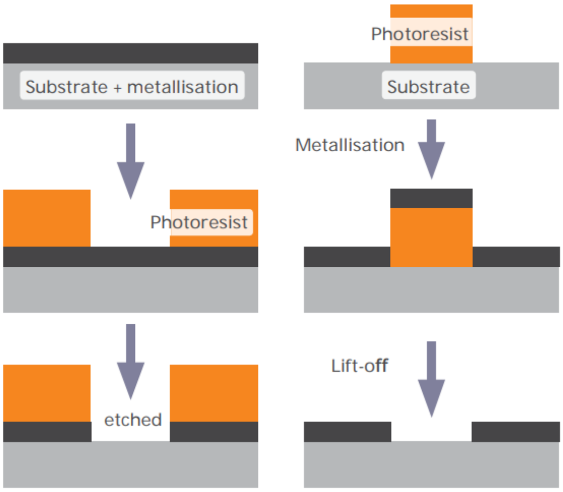

Figure 2.8: Comparison between etching (on the left) and lift-off (on the right) processes [31]

the sites not protected by the resist. A layer of metal is deposited on the whole patterned substrate, but after resist removal only the sections that were deposited on the exposed substrate remain on the sample. The two techniques are depicted in figure 2.8.

Resist strip After etching or metallisation of the sample the resist needs to be removed. Again two main methods of stripping are present: wet stripping, in which an organic or inorganic solution is used to dissolve the resist, or dry plasma etching. A common and inexpensive stripping solution is acetone, which can however leave residues on the surface and is therefore substituted with specialized strippers in industrial applications.

2.2.1 Image reversal photoresist

Image reversal photoresists are a special class of photoresists that can behave either as positive or negative resists depending on the processing conditions. If developed right after the exposure they act as positive resists, while they can be further processed to act as negative ones. The complete process, detailed in [31], will now be explained and is depicted in figure 2.9.

1. Substrate preparation, resist deposition through spin-coating and soft baking are performed as for standard photoresists.

2. Sample exposure through a photomask (step **(1)** in figure 2.9): at this point the exposed resist is soluble, so if the sample is placed in the developer the obtained pattern would be the same as the one for a positive photo-resist.

3. Reversal bake (step **(3)** in figure 2.9): the sample is baked, at a higher temperature than in the soft-bake step, in order for the exposed sections of the resist to cross-link and become insoluble in the developer; the unexposed parts remain photoactive.

4. Flood exposure (step **(4)** in figure 2.9): the sample is illuminated again by UV light but in this case without any mask placed between the lamp and the substrate. Therefore the previously unexposed resist becomes soluble while the cross-linked sections remain unaltered.

5. Development (step **(6)** in figure 2.9): after the development step only the cross-linked sections remain, forming a pattern which would correspond to the use of a negative photoresist.

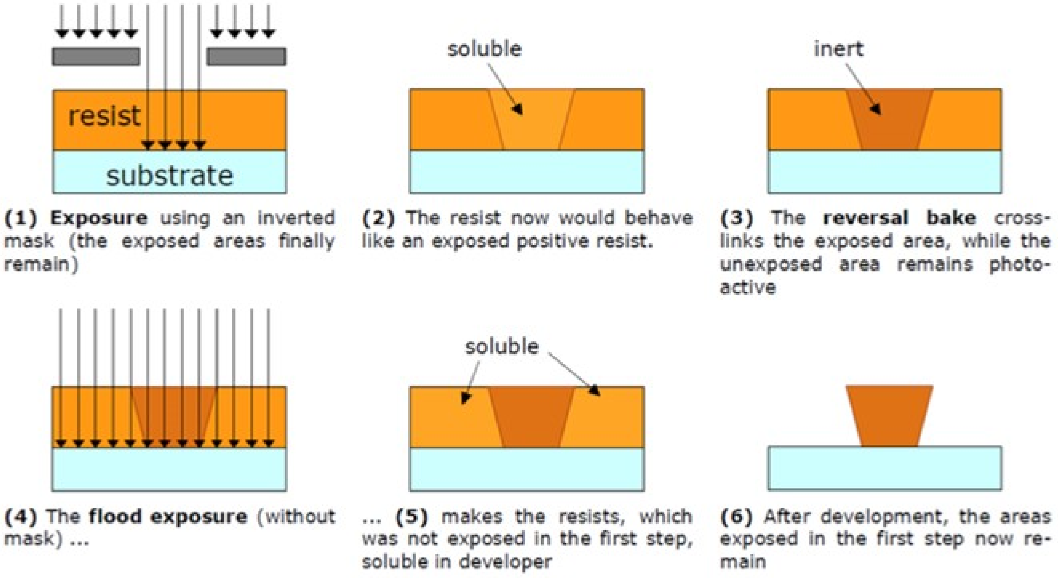

(1) Exposure using an inverted mask (the exposed areas finally remain)

(2) The resist now would behave like an exposed positive resist.

(3) The **reversal bake** cross-links the exposed area, while the unexposed area remains photo-active

(4) The **flood exposure** (without mask) ...

... **(5)** makes the resists, which was not exposed in the first step, soluble in developer

(6) After development, the areas exposed in the first step now remain

Figure 2.9: Processing steps for image reversal photoresists[31]

Image reversal resist is useful since the same resist can be used both in positive and negative modes, reducing the necessary optimization processes. However, its main application is in the lift-off technique, thanks to its profile.

Indeed when metal is deposited on top of a positive resist (left side of figure 2.10), whose edges have a positive inclination, it forms a continuous film across the whole surface, making the selective removal of the metal only from zones covered in resist quite difficult. On the other side, metal evaporated on negative-profile resist doesn't form a continuous film, but the sections of metal which are deposited on the substrate are vertically separated from the sections deposited on the resist. Therefore during resist stripping it's possible to cleanly remove only the metal which was deposited on the resist, without lifting off also the sections that are supposed to remain and without leaving any residual metal along the edges. Image reversal photoresist processed in the negative mode acquires also the negative profile of this class of resists, and can therefore be successfully used for the lift-off technique.

Other positive features of image-reversal resist are the fact that the degree of undercut can be tuned by varying the first exposure dose and image reversal baking temperature [32], and that the image-reversal resist isn't subjected to the swelling problems that can reduce the resolution of standard negative resists.

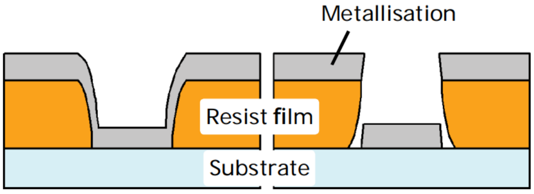

Figure 2.10: Metal deposition on positive (left) and negative (right) photoresist. It can be seen how in the positive case the metal film is continuous, while in the negative one the sections on the substrate can be separated from the sections on the resist. [31]

2.3 Cell division in CIGS solar cell

It has been explained how the fabrication of CIGS solar cells happens through multiple coating steps, in which the different layers are deposited either trough sputtering, evaporation and chemical bath deposition. These deposition techniques, in particular CBD, are often isotropic, so that thin layers of the buffer and oxides materials are deposited also on the sides of the samples, and not only on the surface. This leads to electrical contacts between the molybdenum back contact and the front oxides, preventing the cell from working. Therefore it is necessary to separate the surface of the samples from its side, so that this connection is removed [33].

At laboratory scale the surface is not simply isolated from the side, but it is also divided in smaller sub-cells, in order too increase the lateral conductivity of the cell and reduce the number of possible defects created by inhomogeneities in the sample.

The most commonly used technique for the separation of small area sub-cells is mechanical scribing. In this case a needle or a fine blade is dragged on the surface of the complete cell (see figure 2.11a) in order to carve the layers. Both the window layers and the CIGS are removed, as indicated in figure 2.11b. This process is simple, fast and inexpensive, but it can cause unwanted chipping and damage in the area surrounding the incision. Moreover, the edges of the scribed lines aren't sharp and the lines' thickness is not constant, especially at intersections between perpendicular lines. [4]. A possible alternative consists of separating the subcells by removing sections of the window layers through chemical etching. In this case photolithography can be used to create a photoresist pattern on the surface of the cell, so that during the etching process the areas covered by resist are preserved [4].

By employing the etching technique, only the window layers are removed (see figure 2.11c), so that at the end the surface presents square or rectangular complete cells separated by stripes in which the CIGS is exposed.

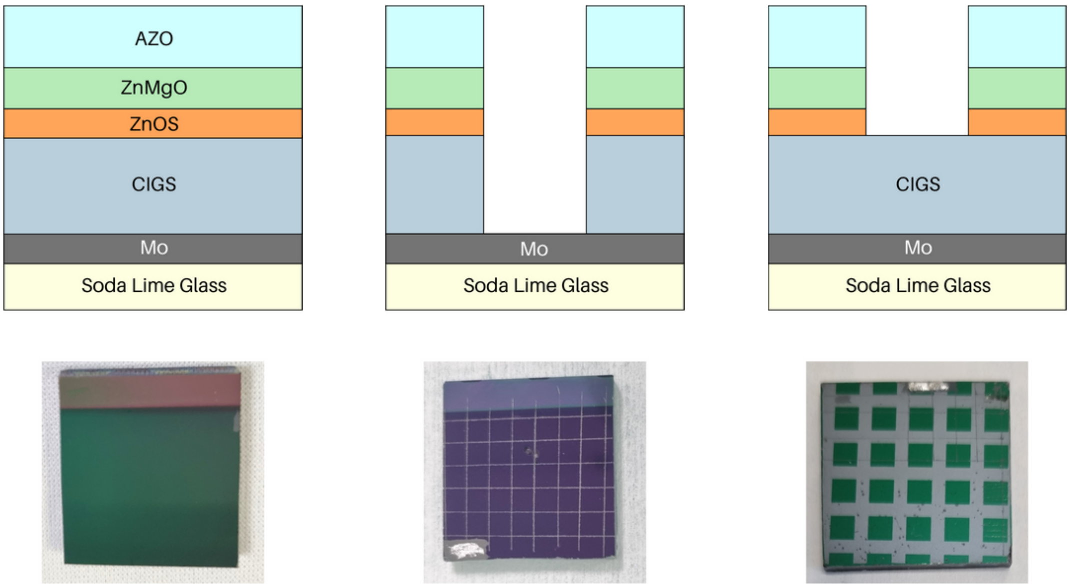

(a) Layers and picture of complete cell

(b) Layers and picture of cell after division by scribing

(c) Layers and picture of cell after division by lithography

Figure 2.11: Difference in the division of a CIGS cell in small area subcells through mechanical scribing or photolithography-assisted chemical etching. The grey areas correspond to CIGS meanwhile the window layers appear green or purple.

For clearness of notation, in the following the process of separation of sub-cells through mechanical scribing will be simply noted as 'scribing' process. On the other hand, the separation of subcells performed by chemical etching of the window layers, whose surface has been covered with photoresist and patterned through photolithography, will be indicated by the term 'lithography'.

This thesis work aims to test and optimise the photolithography process for subcell separation. Photolithography is indeed a promising technique since it will allow to selectively etch only the window layers, leaving the CIGS layer undamaged. Moreover the lateral resolution of lithography is expected to be much greater than the one of scribing, allowing to obtain sub-cells with precise dimension. Additionally, if the process is performed successfully, no chipping or damage of the sections adjacent to the etching sites will be present.

2.4 Contact application

In very small-area cells, like the $0.1\,cm^2$ cells that will be later described, the transparent conductive oxide layer is sufficient for efficient carrier collection and transport. However, it is found that in larger cells, $0.5\,cm^2$ or more, better efficiencies are found with the addition of top metal grids on the surface of the cells, with the configuration shown in figure 2.12a. [34]. The grids are indeed composed of materials with very high conductivity, which can strongly reduce the resistive losses during charge collection. The main downside of grid application is shading of the underlying layers: being opaque the grid prevents light from reaching the absorber, thus decreasing charge generation, and consequently the cell's J_{sc}. On the other side, the decrease in resistance improves the value of the fill factor of the device. Therefore a careful optimization of the geometrical parameters of the grids is necessary.

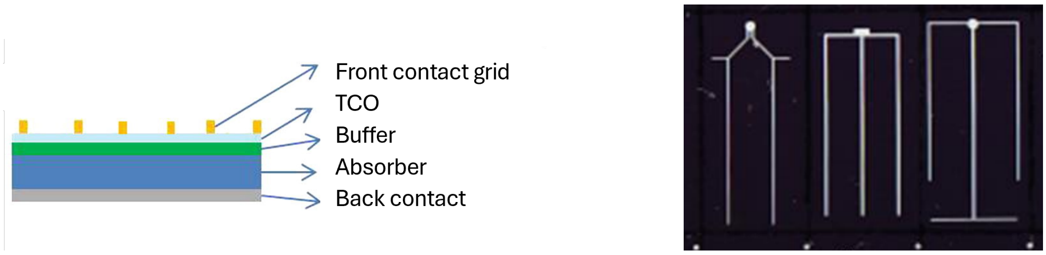

(a) Scheme of the cross-section of a CIGS cell presenting both a TCO top contact layer and metal contact grids (adapted from [34])
.

(b) Proposed designs for top grids for small area CIGS cells (adapted from [35])
.

Figure 2.12: Structures of CIGS solar cells with top contact grids.

In small-area cells, grids usually present a contact pad on which thin parallel fingers are connected, with different possible designs, like the ones shown in figure 2.12b. In particular, wide grids that are densely disposed on the surface lead to higher charge collection, but also to higher shading. Grids with higher thickness, up to 50 μm, ensure higher charge collection without increasing the shaded surface, but from a fabrication point of view require higher use of material and more complex deposition techniques. Finally, the cell length, and therefore the grid length, influence the fill factor, with longer cells leading to lower FF [36].

Contact grids for wide area cells and modules are commonly deposited through screen printing of silver or aluminium paste [24]. For laboratory scale applications other methods can be used, like metal evaporation through a mask, presenting the grid pattern, or evaporation on a substrate coated with resist patterned by photolithography.

2.5 Techniques for solar cells characterization

The structure and performances of solar cells can be characterized by many different techniques of various complexity and specificity. In the following, the theoretical background of the main techniques later employed in the experimental work is described. Both morphological, elemental, and opto-electronic analysis techniques are presented.

X-ray fluorescence X-ray fluorescence (XRF) spectroscopy is a technique which allows the identification of elements present in a sample probed by X-rays.

X-ray fluorescence is a phenomenon that occurs following a photoemission event. When a photon with energy comparable to the binding energy of a core electron, typically in the X-ray range, interacts with an atom, the core electron can acquire enough energy to be ejected, thus ionizing the atom and leaving a vacancy. This vacancy can then be filled by an electron from an outer shell. The difference in energy between the two orbitals can finally be released in the form of X-rays, which will have lower energy than the original incoming ones (Figure 2.13).

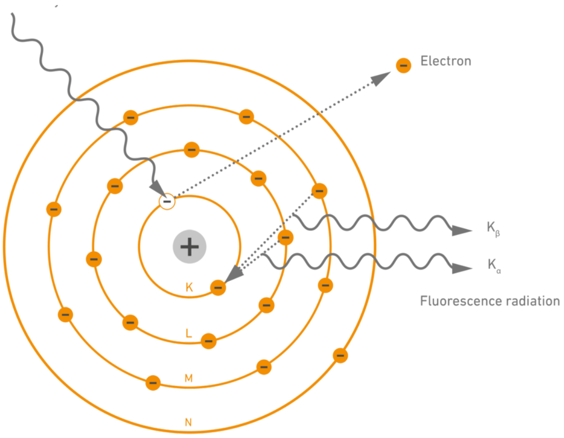

Figure 2.13: Schematic representation of the photo-emission phenomenon leading to X-ray fluorescence [37].

The emitted radiation, being dependent on this difference between energy levels, is highly characteristic of the element that has been excited. Therefore by probing the sample with incident X-rays of varying wavelengths and acquiring the emitted radiation, it is possible to obtain an X-ray fluorescence spectrum. It presents peaks in correspondence to the wavelengths of the characteristic emitted radiation, which can then be compared to tabulated values to identify the elements composing the sample [38].

Profilometer Profilometers are instruments able to determine the depth profile of sample surfaces. In particular, they can be used to determine depth differences between adjacent sections of a sample or to obtain a measurement of the roughness of a surface.

They consist of a stylus with a round tip, which can vary in diameter between 0.1-2.5μm, which is dragged across the surface of the sample at a constant speed and with a constant applied force. The vertical movement of the stylus is detected either by a differential transformer, by an optical sensor or by a capacitance sensor. It is then amplified and digitized, giving as an output the vertical displacement as a function of the stylus position [39].

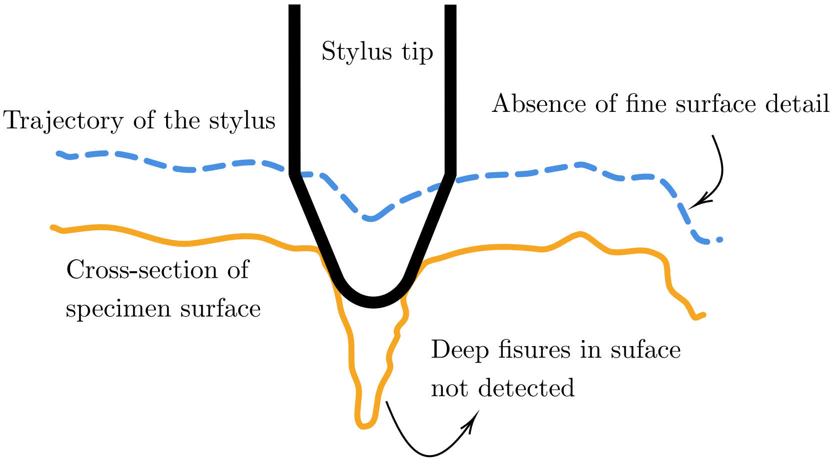

Figure 2.14: Representation of the profilometer stylus scanning a rough surface, adapted from [39].

Mechanical profilometer allow fast and simple surface measurement with high sensitivity. Their main downside is the possible scratching of the surface, especially for softer metals or polymers at high speeds. Moreover, due to the finite size of the tip, they can't register surface concavities smaller than the radius dimension, which can lead to registered surface profiles smoother than in reality, as visible in figure 2.14. In this work the profilometer is used exclusively for measuring depth variation between different areas of the cells, therefore this phenomenon does not affect appreciably the final results [40].

Glow discharge optical emission spectroscopy Glow-discharge optical emission spectroscopy (GDOES) is a technique which allows the determination of the elemental composition as a function of depth. It combines a glow discharge plasma source with high resolution optical spectroscopy, so that elemental analysis and depth profile can be obtained simultaneously. The instrument is based on a pulsed radio frequency plasma which is inserted in a tube that acts as the anode (see figure 2.15). The plasma, most commonly made of argon (Ar), is first used to sputter the surface of the sample, which acts as a cathode. The sputtered atoms diffuse away from the sample surface, are excited by collision with the plasma itself and then, during relaxation, emit photons with energies characteristic of the material. This light is collected and analyzed by an optical system. An interferometer is also present to determine the thickness of the sputtered layer. Since new material is continuously eroded, it is possible to obtain different spectra corresponding to different depths [41].

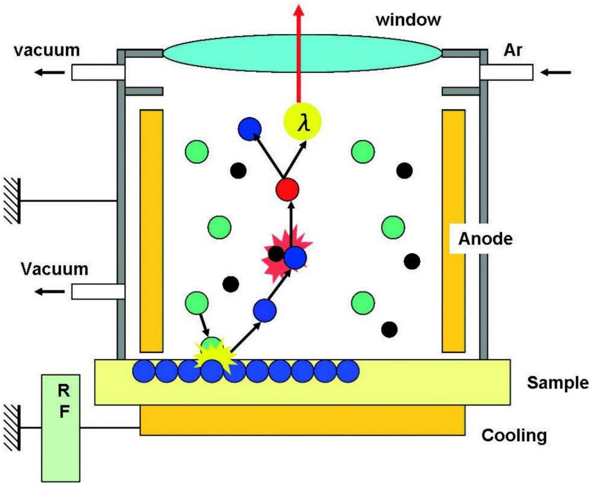

Figure 2.15: Schematic representation of the working principle of a GDOES instrument (adapted from [42]).

Scanning electron microscopy Scanning electron microscope (SEM) is a powerful imaging technique based on the irradiation of a sample with an electron beam. Multiple interaction processes are possible between the electrons and the sample, but electron microscopes are mostly based on two of these signals: secondary electron (SE) and back-scattered electrons (BSE). Secondary electrons are extracted from the surface of the sample, at a maximum depth of a few nanometers and they have low energy, conventionally less than 50 eV. The number of collected electrons depends on the morphology of the surface and on the incidence and collection angles, therefore the secondary electrons give information on the surface topography. Back-scattered electrons derive instead from elastic collisions with the atomic nuclei. Their energy, higher than the one for SE, is strongly dependent on the atomic number Z. Therefore BSE can be used to create a map of the elemental composition of the sample [9].

Another analysis that can be performed in a SEM equipment is energy dispersive X-ray (EDX) spectroscopy. This technique is based on the detection of X-rays generated after the sample is hit by the electron beam. Indeed, if the incoming electrons are sufficiently energetic, they can cause the emission of a core electron from an atom of the sample. The empty state is then occupied by another electron originally in a higher level and the excess energy can be emitted as X-rays. The energy of this radiation is characteristic of the target composition and can therefore be used to obtain the sample elemental composition [43].

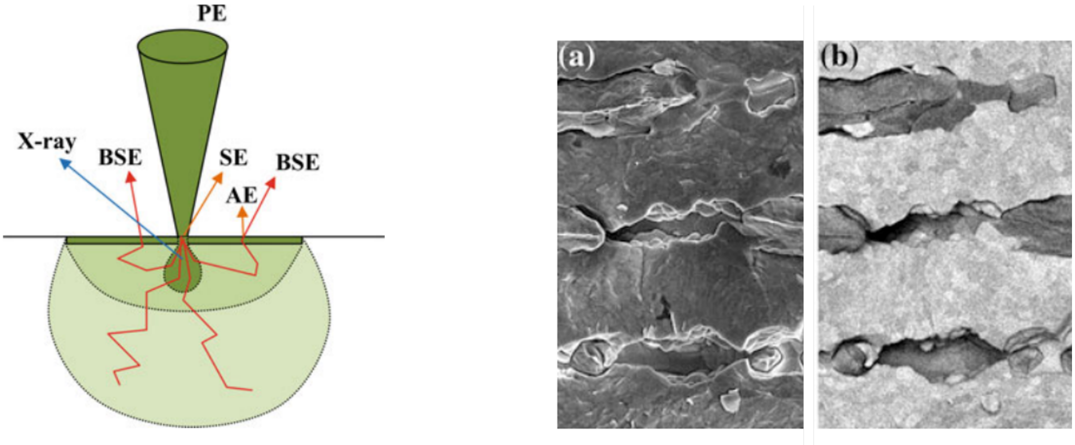

(a) Principal interaction processes following irradiation of a sample with an electron beam

(b) SE image of ceramic capacitors, where the surphace morphology is visible (a) and corresponding BSE image with elemental information (b)

Figure 2.16: Principal SEM imaging signals, adapted from [43]

External Quantum efficiency EQE is defined as the number of photon collected per photon incident on the solar cell:

$$EQE(E) = \frac{1}{q}\frac{dJ_{sc}(E)}{d\Phi(E)} \tag{2.3}$$

where $d\Phi(E)$ is the incident photon flux in the energy interval dE $[\Phi] = cm^{-2}s^{-1}$.

EQE measurements are useful to obtain information about the origin of loss mechanisms which limit the performance of a solar cell. Indeed in the ideal Shockley-Queisser limit case, it would be $EQE(E) = 1$ for photons with $E \geq E_g$ and $EQE(E) = 0$ for $E < E_g$. In real cells, however, the external quantum efficiency is lower than one even for sufficiently energetic photons. This can happen due to optical losses, caused either by reflection or parasitic absorption, or due to recombination losses. These phenomena will impact different sections of the EQE spectrum, making it possible to identify them.

An EQE apparatus usually consists of a light beam, produced by a tungsten or xenon lamp, which passes through a chopper and a monochromator. The monochromatic beam illuminates a small spot on the cell surface in order to test the cell response at different wavelengths. The output signal is then converted to a voltage and amplified through a lock-in amplifier, whose reference signal is provided by the chopper [9].

Chapter 3

Experimental process

3.1 Samples

The sub-cell separation process was applied to complete solar cells previously fabricated at the IPVF laboratories. All experimental processes and characterizations where performed in a clean room with controlled temperature and humidity.

The most commonly used samples present the following structure:

- **Substrate**: 3 mm SLG substrate, cleaned with argon plasma etching.
- **Back contact**: 800 nm Mo deposited by sputtering with Ar plasma.
- **CIGS**: 2000 nm standard band-gap (1.18 eV) CIGS, deposited through three-stage co-evaporation at 550 °C.
- **Buffer layer**: 30 nm ZnOS deposited by CBD at 80°C for 8 minutes. The deposition solution is composed of thiourea ($SC(NH_2)_2$), zinc sulphate ($ZnSO_4$) and ammonia (NH_3).
- **Front contact**: 50 nm ZnMgO followed by 350 AZO deposited by sputtering in an Ar/O_2 plasma.

Cells with other two designs where also processed, differing from the standard structure for the buffer layer composition and for the top contact deposition method. One case presents cells with the structure: SLG/Mo/CIGS/ZnOS/i-ZnO/AZO, where the difference lays in the use of i-ZnO instead of ZnMgO as the first transparent conducting oxide. The i-ZnO is deposited by ALD at different temperatures, ranging between 120°C and 180°C, and presents a thickness that can be set between 10 nm and 50 nm. In the other case the buffer layer is substituted by CdS, deposited too by chemical bath deposition and with a thickness of 50 nm, while the first oxide is made of 50 nm of i-ZnO, deposited through sputtering. The total cell structure is therefore: SLG/Mo/CIGS/ZnOS/i-ZnO/AZO.

3.2 Experimental steps for cell division through photolithography

In order to divide the surface of a sample in sub-cells through photolithography different steps are needed. First the resist has to be deposited and a pattern has to be created in it through exposure to UV light. Then the sample needs to be submerged in an etchant solution, so that the window layers are removed from the exposed areas while they are preserved in the zones covered by the photoresist. Finally, the photoresist has to be removed with a lift-off solution in order for the cell to be ready for testing.

3.2.1 Photoresist deposition and patterning

The AZ5214 photoresist from Merck was used for this process. This resist was chosen since it is an image reversal photoresist (see section 2.2.1), which is optimal for the lift-off technique needed for grid deposition; it also produces thin films (1-2 μm) and provides good lateral resolution ($< 1 \mu m$).

The photolithography parameters have been adapted from previous protocols applied on different classes of solar cells. In particular they had to be modified from the ones suggested by the supplier ([44]) to account for the thick glass substrate used for CIGS, instead of the thin silicon wafer on which protocols are usually based.

In order to align the mask to the substrate and expose the resist, the Süss MicroTech MA6 aligner was used. This instrument contains a moving stage with a mask holder and a sample holder, an optical microscope, and a UV lamp, as shown in figure 3.1. Both sample and mask holder are equipped with vacuum systems to keep the two elements in place during the exposure. The x-y position of the sample with respect to the mask can be finely tuned with two knobs and the alignment can be checked through the optical microscope. A digital camera is connected to the microscope, so that the surface of the sample can be seen from a screen and pictures can be exported. The UV lamp is a 1000W mercury arc lamp, cooled by nitrogen, which can emit in the 365-435 nm range. For the AZ5214 exposure a wavelength of 365 nm is chosen (i-line). An optical system ensures the transmission of the light from the lamp to the sample.

The sample holder can also move along a vertical axis, in order to reach the correct distance from the mask during the exposure process. This distance depends on the chosen operation mode, either contact, which is chosen for the sub-cells division, or proximity. Projection exposure is not available for this aligner model [45].

Since the photoresist is sensitive to UV light, the process is entirely performed in a room in which only yellow lights are present. At the beginning of the process the cell presents a uniform surface, as in picture *a* of figure 3.2.

The experimental steps used for the resist deposition and patterning are the following:

- **Cell preparation**: Thanks to the intrinsic roughness of the CIGS solar cells win-

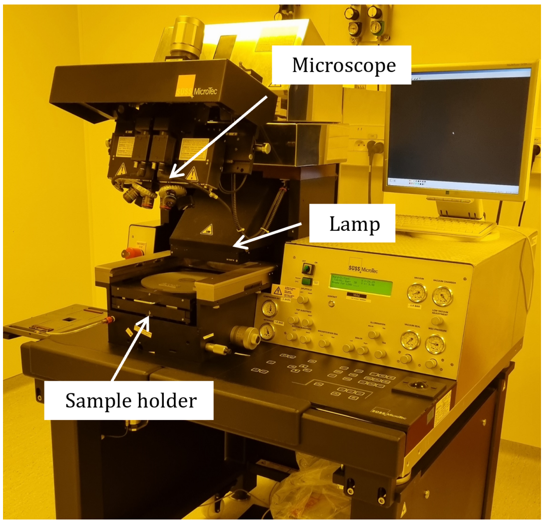

Figure 3.1: Süss MicroTec MA6 aligner. The sample holder, the lamp and the microscope are highlighted.

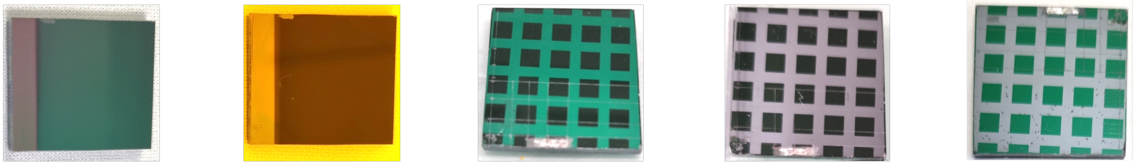

a) Complete cell b) Resist deposited c) Resist developed d) Window layer etched e) Resist removed

Figure 3.2: Samples during the various sub-cells separation steps.

dow layers there is no need for a thorough cleaning procedure before the resist deposition. Similarly the deposition of an extra adhesion-enhancing layer is not necessary. It is however still important to put the cells through a water evaporation step in order to eliminate as many water molecules as possible from the cell surface. Indeed the presence of excess water can cause detrimental reactions with the photoresist. The cells are therefore placed on a *VWR 720 advanced* hot plate for 3 minutes at 123°C. After this time the cells are transferred onto a metallic surface for cooling.

- **Resist deposition**: The AZ5214 photoresist is deposited by spin coating on the surface of the samples. This process is performed with a Laurell spin coater, model WS-650 Hz-8NPP, for 30 seconds at 4000 rpm.
- **Soft baking**: The samples are placed on the hot plate for 3 minutes at 123°C. The temperature is continuously controlled through a FLIR-E63900 thermoscanner, in order to assure a homogeneous heating of the samples. The samples are then placed

on a metallic surface for cooling and re-hydration.

- **Exposure through photolithography mask**: the mask chosen for cell division presents a pattern composed of $0.1\,cm^2$ transparent squares separated by 2 mm wide opaque lines (see figure 3.3a). Since at the end of the process the AZ5214 resist behaves as a negative resist, the squares will remain in the resist while the lines will be dissolved. The mask and the sample are loaded in the aligner and their relative position is tuned in order to obtain as many complete sub-cell as possible from the substrate. The sample is exposed for 3 seconds in 'hard contact' mode.
- **Hard baking**: the sample is placed again on the hot plate at 127°C for three minutes. For this step, maintaining a stable temperature (without any variation exceeding 1°C) is crucial. Indeed, if the temperature is too high, also the unexposed resist will become insoluble, leading to a final sample covered in a uniform layer of resist. On the other hand, if the temperature is too low, the cross-link process does not take place and during development all resist is removed. When the time is concluded the sample is removed from the hot-plate and cooled down.
- **Flood exposure**: The cell is placed again on the aligner's sample holder and the photomask is removed. The sample is exposed for 35 seconds in 'flood' mode so that the whole surface is uniformly illuminated.
- **Development**: The sample is submerged in the Merck AZ 2026 MIF developer and, with the help of a strainer, it is continuously rotated to obtain a uniform development across the surface. It is kept in the solution for one minute, then it is rinsed in deionized water and dried with N_2 gas.

At this point the sample has the appearance visible in figure picture *c* of figure 3.2: the black resist covers the square subcells that will remain intact after the etching process, meanwhile in green are visible the sections of the window layer that will be removed in order to separate the subcells.

3.2.2 Etching

Once the pattern has been created it is necessary to remove the window layers by etching the samples with a hydrochloric acid (HCl) solution. HCl is chosen since it is a known etchant for zinc-based oxides. Additionally it does not react with CIGS, making it an ideal solution to etch only the cells' window layers while keeping the absorber unaltered.

The samples are submerged, one at a time, in 40 mL of 10^{-2} M HCl for 2.5 minutes. They are held with a pair of cleaving pliers, as shown in figure 3.3b, and continuously moved inside the solution in order to obtain a uniform removal of the window layers. Afterwards they are submerged in deionized water, in order to interrupt the etching process and remove any trace of acid, and then dried with N_2 gas.

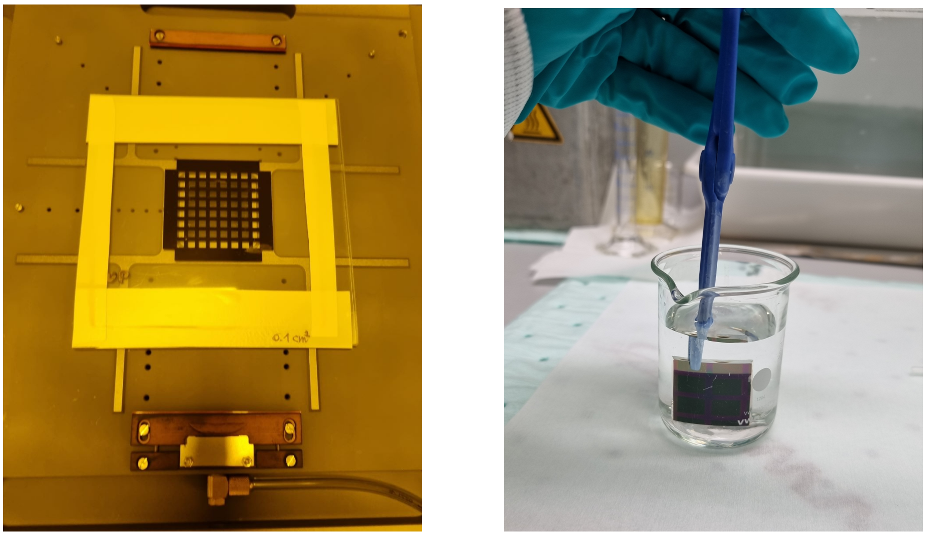

(a) Mask for the 0.1 cm^2 sub-cells division, loaded in the aligner mask hold.

(b) Cell submerged in the HCl solution for window layer etching.

Figure 3.3: Cell division process.

The acid concentration and the duration of the etching are the key parameters of the process, which need to be carefully optimized. Indeed a too low etching power or duration would result in an incomplete and non-uniform etching of the window layers, with some oxides remaining on top of the absorber. This would lead to the failure of the process, since the subcells would not be properly separated. On the other side a too high etching power or time would lead to under-etching, the situation in which the acid solution is strong enough to diffuse below the resist and remove part of the features that had to be preserved.

By gradually etching the samples for increasing time and concentrations it was possible to determine the reported optimal etching conditions. The procedure and detailed results of these tests are reported in section 4.1. At the end of the etching step the surface of the cell appears as in picture *d* of figure 3.2: the black squares are the areas in which all layers have been reserved by the photoresist, still present, meanwhile the gray lines are the CIGS.

3.2.3 Resist removal and contact application

Since the patterned resist is no longer needed and it interferes with the correct functioning of the cells it has to be removed. This is done by submerging the samples in acetone for 30 seconds, stirring continuously, and then rinsing them with deionized water and drying them with N_2 gas. Now the surface has the final look visible in the last picture of figure

3.2: square complete cells (in green) are separated by stripes in which the window layers are removed and so the CIGS layer is visible (in gray).

Lastly, in order to measure the opto-electronic properties of the cells, a contact point needs to be created with the molybdenum layer. Therefore a small section of the CIGS is scraped with a blade to uncover the underlying molybdenum, and indium paste is applied to this area, with the help of a soldering iron, to form the contact.

3.3 Experimental steps for front contact application

In order to optimize the charge collection in larger area subcells ($0.5\,cm^2$ or more), it is useful to apply contact grids on top of the AZO layer (see section 2.4). Indeed the resistivity of metals is much lower than the ones of the conductive oxide, leading to more efficient charge collection and transport to the external circuit, especially for cells integrated in modules.

The standard process for grid deposition consists in direct evaporation of the metals on the substrate through a mask, patterned with the desired design for cells and contact pads. The evaporation takes place in a PLASSYS MEB 550SL electron beam evaporator, which presents six evaporation chambers, useful to deposit sequentially different materials, and which operates at a vacuum level of 10^{-7} mbar. The total grids are composed of three layers: 50 nm of nickel, 600 nm of aluminium, 50 nm of nickel. Aluminum presents optimal transport properties but it is easily subjected to oxidation, therefore a thin layer of nickel is added to protect the aluminium layer and to improve the adhesion to the window layer. The mask used for grid deposition has been optimized for the $0.5\,cm \times 1.0\,cm$ sub-cells divided by scribing; it presents two fingers and a contact pad (see figure 3.4a).

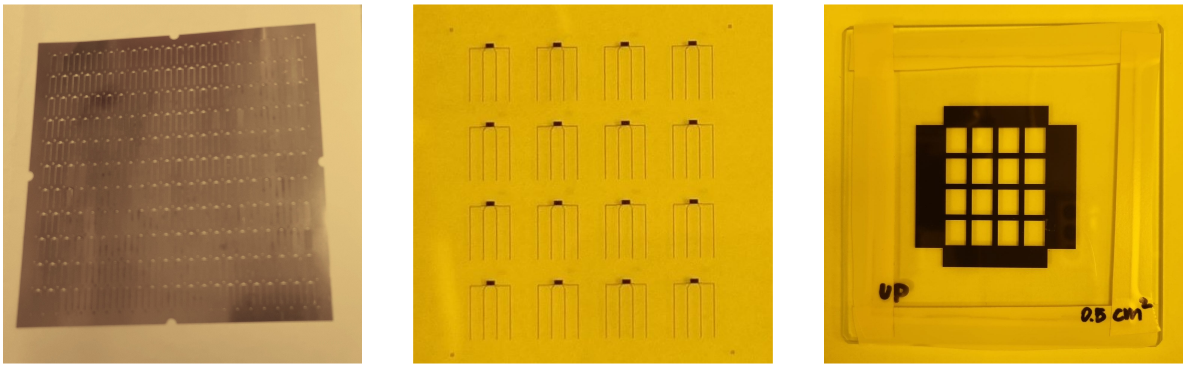

(a) Mask for the deposition of grids in the evaporator chamber.

(b) Lithography mask for the grid pattern

(c) Mask for the $0.5\,cm^2$ sub-cells division.

Figure 3.4: Mask used in fabrication if cells with grids

The suggested procedure including the use of photolithography requires too the evaporation of the metals composing the contact, but no mask is placed in the evaporator. Instead the Ni/Al/Ni layers are deposited uniformly on the whole sample, which is previously coated with a top resist layer patterned through lithography, with the areas not covered by resist corresponding to the shape of the grids. In order to obtain these features the photolithography process needs to be performed two times: first to create the pattern for the grid evaporation and then to divide the subcells. The complete process is the following:

- **Resist deposition with grid pattern**: a first layer of resist is deposited and patterned following the procedure described in section 3.2.1. The only difference lies in the mask used in the first exposure step, which is not the one for $0.1\,cm^2$ subcells but presents the top grid design shown in figure 3.4b. Keeping a constant hard baking temperature is even more crucial in this case. Indeed if the temperature is too high also the non-exposed or weekly exposed resist will begin to cross-link, reducing the size of the already thin features of the grids. This will prevent the subsequently evaporated metals from properly adhering to the AZO surface. At the end of the process, the cells will have the appearance of picture *b* of figure 3.5
- **Grid metal deposition**: the samples are loaded in the PLASSYS MEB 550SL electron beam evaporator without inserting any mask in front of the samples. A sequence of 50 nm nickel, 600 nm aluminium and 50 nm nickel is evaporated on the substrate in the vacuum chamber (see picture *c* of figure 3.5).
- **Lift-off**: in order to remove the layer of resist used to deposit the grids, the samples are placed in a Becker containing acetone. Since the surface is now coated with the metal layer, much longer time is needed for the solvent to dissolve the photoresist. The samples are therefore left in the closed container for 30 minutes. The residues of the metal film are then peeled from the surface with the help of a pipette. The cells are then rinsed with deionized water and dried with nitrogen gas, and appear as in picture *d* of figure 3.5.
- **Resist deposition with sub-cell pattern**: following again the same procedure with unchanged parameters, the samples are heated for water evaporation, covered in resist by spin coating and placed on the hot plate for the soft baking. Then they are transferred to the aligner in which a photomask presenting a pattern for rectangular sub-cells with an area of $0.5\,cm^2$ is loaded (see figure 3.4c). This mask is designed to match the geometrical parameters of the grid pattern. Therefore a careful alignment procedure is necessary, in order to position each grid in the center of every sub-cell. It is then possible to proceed with the exposure, the hard baking, the flood exposure and the resist development.

- **Etching**: The samples are etched in 10^{-2} M HCl for 2.5 minutes, following the procedure outlined in section 3.2.2. Since the resist rectangles are centred on the grids, the grids themselves are protected from the acid and they are not damaged during the etching procedure.

- **Resist removal**: the samples are submerged in acetone for 30 seconds, rinsed in deionized and dried with N_2. Indium contacts are then created as previously explained. The cell presents now the final design visible in picture *e* of figure 3.5, and are ready for opto-electronic characterization.

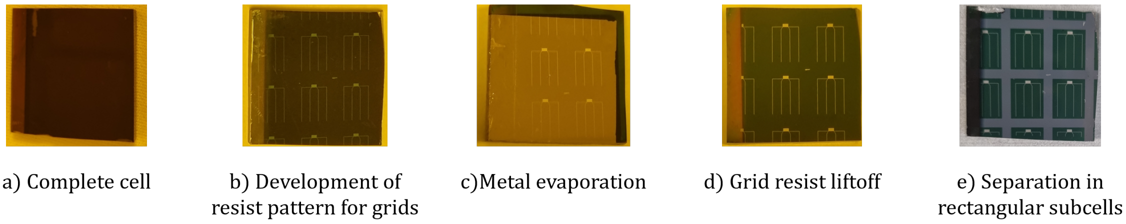
a) Complete cell
b) Development of resist pattern for grids
c)Metal evaporation
d) Grid resist liftoff
e) Separation in rectangular subcells

Figure 3.5: Samples during the grid deposition and sub-cells division through photolithography.

For clarity, the complete process for grid application and sub-cell division is schematized in figure 3.6

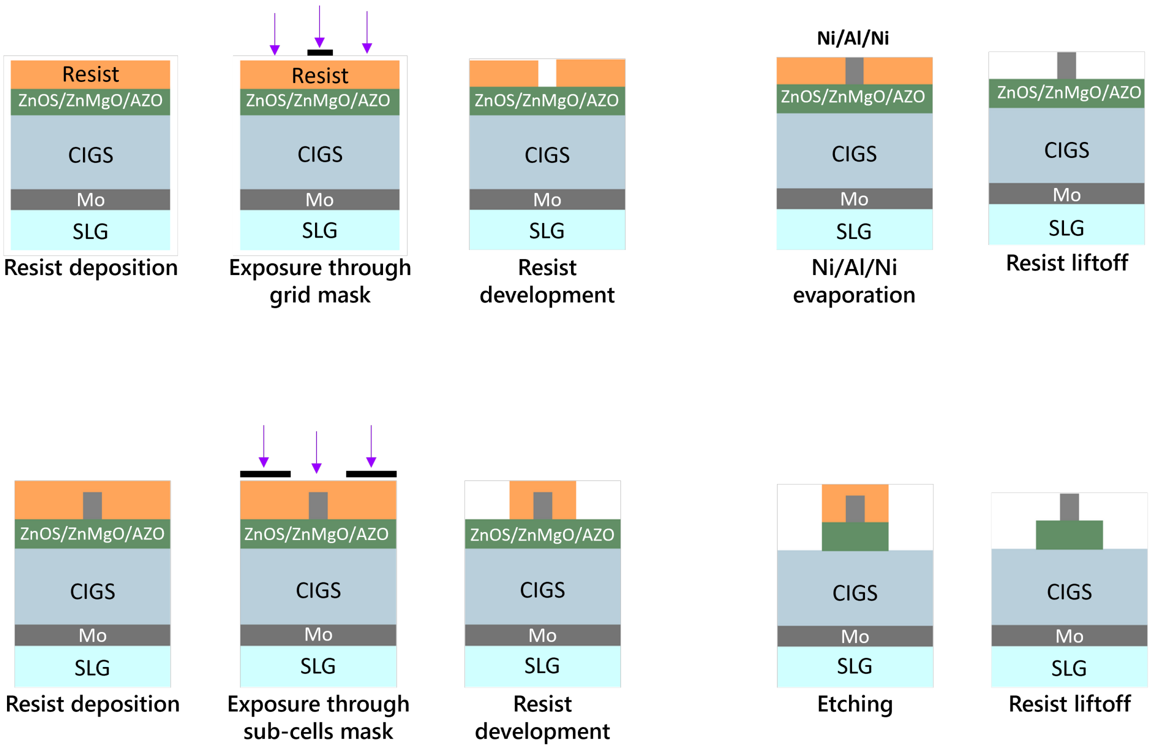

Figure 3.6: Scheme of the experimental steps for grid application and sub-cell division through photolithography.

3.4 Characterization techniques and procedures

In the following paragraphs, the equipment used for the morphological and elemental analysis of the cells is described, and the procedures followed for the different analyses are outlined.

3.4.1 Experimental techniques for morphological and compositional characterization

Profile measurement The depth profile of the samples has been acquired through the *Dektak XT profilometer* by Brucker. It presents a diamond tip which is moved across a line on the sample surface with a stable force, which can be set between 0.098 mN and 147 mN. The maximum available vertical resolution is 0.1 nm and the scan length can be set between 50 μm and 50 mm, depending on the selected range [46].

In particular the profilometer is used to check the thickness of the various layers deposited and then etched through photolithography. The cell is placed on the sample holder and the tip of the instrument is positioned, with the help of the integrated microscope, near the edge of the step to analyze. A scan is then acquired along a line perpendicular to the step border. The employed stylus presents a 2 μm point and exerts a force of 30 mN. The scan is performed at the highest possible resolution, 0.1 nm, available for the 6.5 μm vertical position range and for a scan length of 500 μm.

X-ray fluorescence For elemental characterization the *Fischerscope XDV-SDD energy dispersive X-ray fluorescence measuring instrument* is used. It presents a micro focus tube, with tungsten target and beryllium window; the maximum available voltage is 50 kV. The X-ray detector is a peltier-cooled silicon drift detector with 140 eV resolution. The sample is placed on a moving stage, and the measurement spot can be positioned on the required area with the help of an integrated CCD camera. The instrument can be controlled and the spectra can be analyzed through the WinFTM software [37]. Two kinds of measurements can be performed: qualitative and quantitative. In the qualitative mode the system performs a fast single acquisition and the whole spectrum is shown. It is then possible to visualize the main emission lines for different elements, in order to identify the material composition of the sample. This acquisition mode is useful for the analysis of unknown samples or for checking the presence of a specific element. It does not however provide the quantitative composition of the sample. On the other side, the quantitative measurement mode returns the concentration of specific elements in the sample, given that the expected elements are provided to the software. In this mode each acquisition lasts for 30 seconds, and it is advisable to test different points on the surface in order to reduce the effect of local variations on the sample composition. Both weight percentage and atomic percentage of the elements are given as an output.

Glow discharge optical emission spectroscopy The GDOES analysis allows to obtain the elemental composition of CIGS as a function of the depth of the layer. For this analysis, the Horiba GD profiler 2 is used [42]. This instrument can process both metallic and non-metallic samples thanks to the low-pressure 13.56 MHz RF plasma source, in which argon is used as the sputtering gas. The sample erosion rate is in the 2-10 nm/s range, and the depth resolution can be up to 1 nm. The instrument presents a wide spectral range of 120-800 nm for emitted light acquisition (VUV to IR). The detector is a proprietary High Dynamic Detector, with a dynamic acquisition range of 5×10^9. The sample, which acts as a cathode, is fixed through a vacuum seal in front of the anode, which is a copper tube in which the plasma can flow. The instrument provides as an output the collected light intensity, for each specific wavelength, as a function of the erosion depth. In order to obtain the concentration of the elements in the sample is therefore necessary to calibrate the acquired curve. This is done by using the atomic percentage values obtained by quantitative XRF.

Scanning electron microscope analysis The morphology of the deposited and etched layers has been observed through the ZEISS Merlin VP Compact SEM [47]. The instrument presents a GEMINI electron beam column, which can provide an electron current between 0.02 keV and 30 keV. It contains a *In-lens Duo Detector*, which is able to detect both secondary electron and backscattered electron signals. Moreover it contains a EDX detector for material analysis. The maximum obtainable resolution is 0.8 nm for 15 kV voltages; the factor of magnification ranges between 12 and $2 \cdot 10^6$. The imaging procedure of the CIGS samples has been performed by a dedicated operator.

3.4.2 Experimental techniques for opto-electronic characterization

Current-voltage characteristic measurement In order to acquire the current-voltage (I-V) characteristic of the cell, the sample was illuminated with the Newport Oriel Sol3A solar simulator [48]. This is a class AAA certified simulator, equipped with an external power supply and an integrated shutter. The lamp is a 1000W Xenon arc lamp and a filter is placed in order to obtain a AM1.5 G irradiance. The sample is placed on a platform with an integrated cooling system, to prevent the overheating of the system during long measurements. The cell is then connected, in four probes configuration (see figure 3.7), to the Cicci research Arkeo multi-channel analyzer, which allow the acquisition of the I-V characteristics [49]. Before the beginning of the measurements, the vertical distance between the lamp and the platform has to be calibrated with a reference cell, in order to obtain the certified value of J_{sc}. It is also found (see section 2.1.2), that CIGS solar cells performance increase under illumination [50]. Therefore, before testing, the cells are left under the simulator's lamp for at least 60 minutes. Then two micro-probes are connected to the indium contact and two probes are placed on the corners of a sub-cell, and the current-voltage measurement is started, with customizable voltage range and voltage step. In the case of cells with top contact grids the probes are placed on the contact pad, and not directly on the oxide surface. It is possible to provide to the Arkeo analysis software the value of the area of the sub-cell, in order to obtain directly the plot of the current density J as a function of the voltage. Moreover the system can calculate the main solar cells parameters, namely J_{sc}, V_{oc}, and FF, and derive the efficiency.

Dark current analysis The dark current characteristics was acquired through the BioLogic Sp150 potentiostat (± 10 V, voltage range, 5 μm to 200 mV tunable voltage resolution, 800 mA to 10 μA current ranges, 0.760 nA to 76 fA tunable current resolution) [51]. The cell is connected to the potentiostat in two probe configuration and is covered with a black box to prevent ambient illumination from affecting the results.

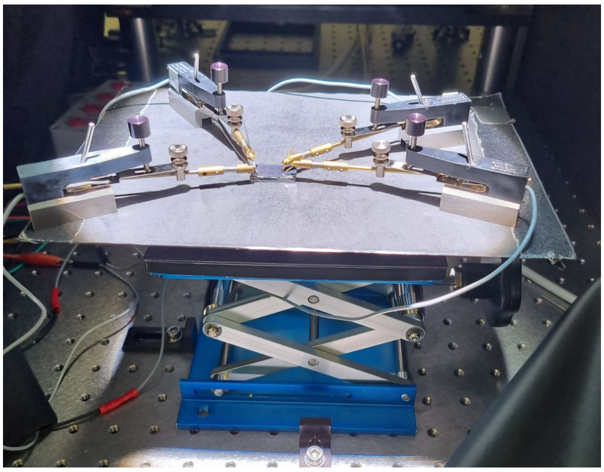

Figure 3.7: Apparatus for the J-V characteristic acquisition.

EQE The EQE spectrum has been acquired through the Oriel IQE 200 quantum efficiency measurement system. It is equipped with a 100 W xenon lamp, a wide area silicon detector and a monochromator. The acquisition can be performed in the 350-1100 nm wavelength range.

The cell is placed on the sample holder and the sub-cell to be analyzed is positioned in correspondence to the instrument's light spot. The sample is connected with two probes, one placed on the indium contact, one on the sub-cell surface, and the acquisition is started. The instrument provides the values of EQE as a function of incident wavelength and calculates the J_{sc} by integration.

Chapter 4

Results

4.1 Validation of lithography process

The first test of the lithography procedure was performed on four cells presenting two different architectures. The first two cells presented the standard stack of layers described in section (3.1): 3 mm SLG, 800 nm Mo, 2 μm CIGS, 50 nm ZnOS, 50 nm ZnMgO, 300 $\div$ 350 nm AZO). In the other two cells, the ZnOS buffer layer was substituted with the same thickness of CdS and the cells were finished by i-ZnO and AZO layers with a total combined thickness of 400 nm. In the following the cells will be indicated with CIGS-ZnOS and CIGS-CdS respectively.

For all the four cells photolithography was employed to deposit the resist pattern for the 0.1 cm^2 sub-cells, by following the deposition, baking, exposure and developing steps described in section 3.2. The resist deposition was successful: the desired pattern was clearly visible and the resist was not peeling off in any unwanted area.

The following measurements aimed to the determination of the optimal etching time for the CIGS cells. Prior to the etching process the profile of the resist was measured with a profilometer, a XRF spectrum of the sample was acquired and a picture of the surface of the cell was taken.

The etching process was performed following the procedure outlined in section 3.2. For this test the solution consisted in 40 mL, 10^{-2} M HCl and the samples were submerged in the solution for 30 seconds before being cleaned in deionized water and dried. At this point the samples were photographed, analyzed through quantitative and qualitative XRF, their images were acquired by a confocal microscope and their surface morphology was measured with a profilometer. After all the analyses were completed, the samples went through another etching stage of the duration of 30 seconds, with the other etching conditions remaining unvaried, and measured again. After each bath in the acidic solution it could be seen that the window layers of the cells were slowly dissolving, starting from the sides of the samples and proceeding towards the centre. This can be seen in Figure 4.1, where the pictures of the surface of one of the cells for increasing etching times are visible. After the first two steps, the CIGS layer (which presents a characteristic light gray colour) was visible at the edges of the sample, as shown in the last four pictures in figure 4.1.

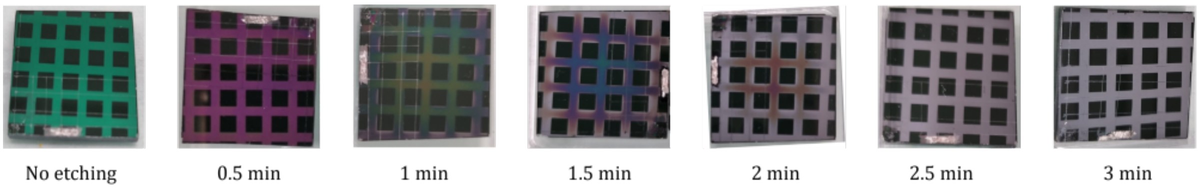

Figure 4.1: Pictures of the surface of a cell for increasing etching time. It can be seen that the window layers start dissolving from the edges of the cell towards the center. After 2.5 minutes, the cell presents a uniformly grey surface. The cell presented the standard ZnOS buffer layer and ZnMgO layer was deposited through sputtering.

This process was repeated six times, for a total etching time of 3 minutes. Indeed, after 2.5 minutes, the samples presented, on the exposed sections, a uniform grey surface that could indicate the conclusion of the etching process. An extra step was added at the end to check the possible effect of an increased etching time.

4.1.1 Profilometer measurements

The profilometer was first used to measure the thickness of the resist layer, by getting the profile of the 'step' between the squares covered in resist and the areas where it was dissolved. In order to account for the thickness difference across the surface (typical of the spin coating deposition process), three different regions were measured for each sample: one on the edge of the cells, one on a corner, and one in the centre. This lead to an average thickness of $h = (930 \pm 30)\,nm$ between the four samples. The high deviation is mostly due to the difference in thickness on the edges of the samples.

After each etching step it was instead measured the thickness difference between the zones where the photoresist was present and the zones where the window layers were being progressively removed (indicated as line 'A' in figure 4.2a). This was done to monitor the thickness of the removed material, expected to be around 450 nm. Again, three zones (one on the edge, one on the corner, and one in the center) were analysed. The profiles before and after etching are shown in figure 4.2b, and the calculated thicknesses for different etching times are visible in figure 4.3. It can be observed that, for increasing etching times, this thickness difference increases until it reaches the expected value and stabilizes after 2.5 minutes. Therefore it was possible to obtain a first validation of the estimated optimal etching time of 2.5 minutes.

To have an additional confirmation of the fact that the exposed layer corresponds to CIGS, before resist deposition a small section of the molybdenum back contact was

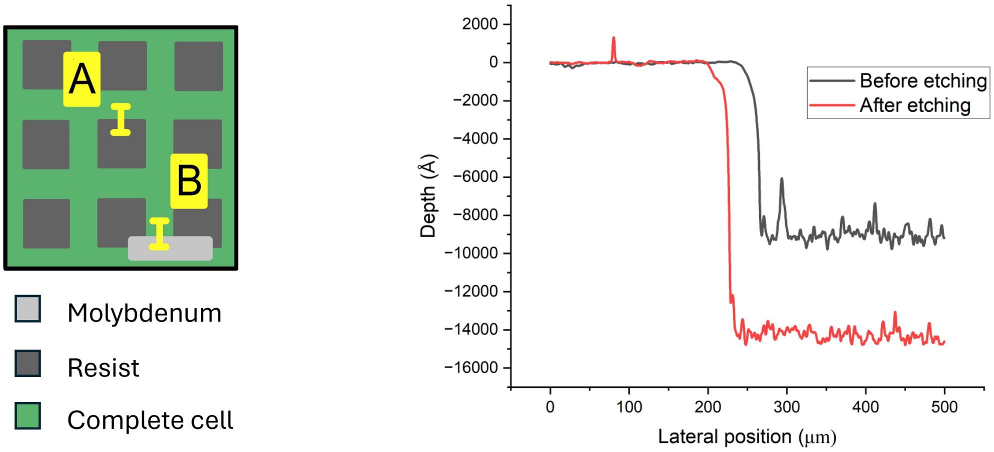

(a) Zones of the sample surface analyzed with the profilometer. The areas not covered by resist are the ones in which the window layers are progressively removed.

(b) Profiles of the border between an area covered in resist and an exposed area, before and after the etching process. The increase of the difference in height in the two zones corresponds to the removal of the window layers.

Figure 4.2: Profilometer scans and their locations

exposed and the difference in height between molybdenum and the complete cell was measured. After the deposition and etching process the thickness difference between molybdenum and what it was presumed being CIGS was acquired, following line 'B' as indicated in figure 4.2a. The values for two cells are reported in table 4.1. It can be seen that the removed window layer thickness is again around 400 nm and that the absorber depth value found after etching corresponds to the expected thickness of CIGS of 2 μm.

Sample	Mo/complete cell	Mo/CIGS	removed thickness
$CIGS - ZnOS\_1$	(2510 ± 30) nm	(2100 ± 20) nm	(410 ± 40) nm
$CIGS - ZnOS\_2$	(2400 ± 20) nm	(2000 ± 10) nm	(400 ± 20) nm

Table 4.1: Values of thickness difference at interface between molybdenum and the complete cell (before etching) and between molybdenum and CIGS (after etching). The variation between these configurations, and so the removed layer thickness, is also reported.

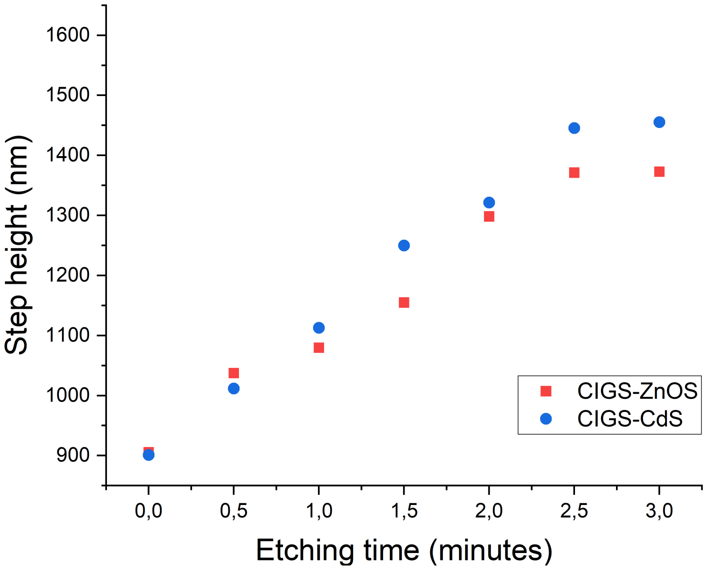

Figure 4.3: Difference in thickness between the areas of the sample covered in resist and the areas where the window layers were dissolving. The values for t=0 correspond to the resist thickness.

4.1.2 X-Ray Fluorescence measurements

In order to check that the chemical composition of the exposed layer correspond to the expected values for the CIGS absorber, XRF measurements were performed.

Before the etching process, a qualitative XRF spectrum was acquired by placing the machine's acquisition point in a central area of the sample not covered by resist. As it can be seen in figure 4.4a for a sample with ZnOS buffer layer, the initial spectrum presents relevant peaks corresponding to molybdenum, from the back contact, to the four elements composing CIGS and to zinc (Zn). The smaller peaks corresponding to zirconium (Zr) and tungsten (W) are caused by the acquisition system and are therefore always present in each spectrum.

On the other side, zinc is contained only in the window layers and its signal can thus be used to track the etching process. It is found that the Zn peak decreases with increasing etching time, until it becomes negligible after 2.5 minutes of etching, as shown in figure 4.4b. The remaining weak signal is caused by the fact that the machine target is not point-like and the features of our sample are small enough for the instrument to sense the presence of zinc in the surrounding areas protected by the resist.

It was therefore shown that the window layers containing zinc were successfully removed during the etching process. In order to check the composition of the now exposed absorber also a quantitative XRF analysis was performed. The values of copper, indium, gallium and selenium concentrations acquired after the etching process were compared with reference values of the raw absorber and are reported in table 4.2, expressed in

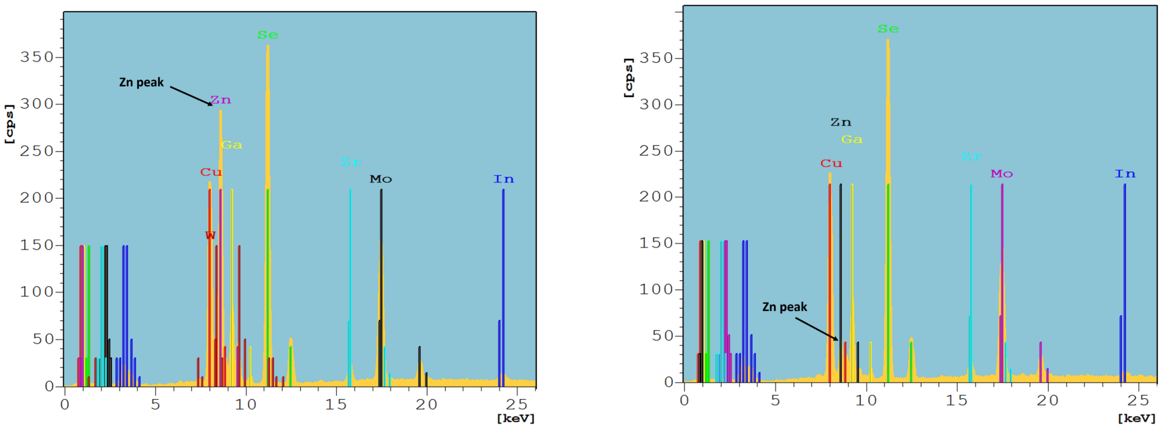

(a) XRF spectrum before etching.

(b) XRF spectrum after 3 min of etching.

Figure 4.4: XRF spectra of an area of the sample not covered in resist, before and after the etching process. It can be seen that the Zn peak, initially very strong, becomes negligible after etching.

atomic percentage. It can be seen how after the etching process the initial values of concentrations are recovered, with very limited variations in the range of 0.5-3 %.

It has to be noted that the reference values were acquired on a section of the full CIGS covered substrate, which was later cut in $2.5\,cm \times 2.5\,cm$ samples. For this test one of these smaller samples was used, which may not correspond to the area originally tested. Since molybdenum and CIGS depositions are not uniform over the whole $10\,cm \times 10\,cm$ glass substrate, small differences in composition and optoelectronic properties can be observed by testing different sub-samples coming from the same original substrate.

Therefore the observed small variations in composition can be attributed to a non-homogeneity of the sample and not to an unwanted effect of the photolithography and etching processes, that are confirmed to preserve the chemical composition of the absorber layer.

Sample		Cu	In	Se	Ga
$CIGS-ZnOS\_1$	raw	23.20	17.96	48.58	10.25
$CIGS-ZnOS\_1$	after etching	23.49	17.30	48.69	10.46
$CIGS-ZnOS\_2$	raw	23.23	13.71	48.62	14.44
$CIGS-ZnOS\_2$	after etching	23.54	12.93	48.90	14.67

Table 4.2: Concentration of CIGS elements acquired by XRF analysis, both on incomplete cells without window layers and on complete cells in which section of the window layers were removed by selective etching. values are expressed in atomic concentrations.

4.1.3 Scanning electron microscope measurements

In order to further check the morphology of the obtained cell and its chemical composition the sample was analyzed by means of a SEM.

In particular the chemical composition of the exposed CIGS layer was obtained from EDX spectroscopy. The resulting atomic concentrations of the $CIGS - ZnOS\_2$ sample are reported in table 4.3.

Sample	Copper (Cu)	Indium (In)	Selenium (Se)	Gallium (Ga)
$CIGS - ZnOS\_2$	25.06	13.10	48.92	13.14

Table 4.3: Concentration of CIGS elements acquired by EDX spectroscopy

A SEM image of the surface of the cell after etching and resist liftoff was also acquired. In figure 4.5 it's visible the sharp separation between the exposed CIGS surface (in the bottom half) and the AZO top layer (top half), which was previously protected by the resist.

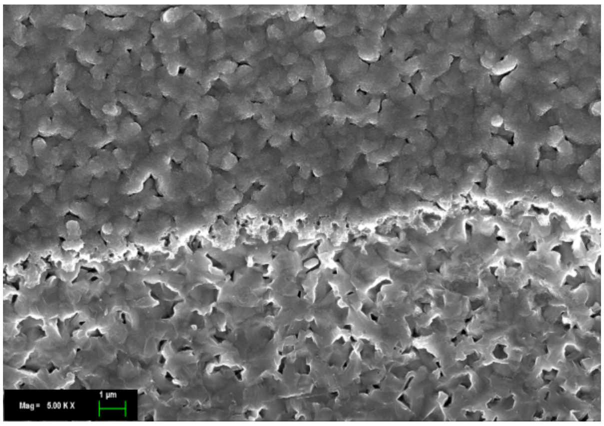

Figure 4.5: SEM image of the surface of the cell after the lithography process. In the top half of the picture it's visible the AZO window layer, meanwhile in the bottom half the underlying CIGS

A common problem of the photolithography process is under-etching, which appears when the etchant solution starts corroding also the area under the resist layer, thus modifying the intended pattern. This can occur if the concentration of the acid is too high or if the sample is kept too long in the etching solution.

Therefore higher HCl concentrations and etching time were tested. A sample which initially measured $5\,cm \times 5\,cm$ was cut into four equal squares. One of these was kept for reference meanwhile the others were subjected to the photolithography process, with varying etching times and acid concentrations. One sample was etched in $10^{-2}M$ HCl for 2.5 minutes, as in previous tests. For the other two samples $5 \cdot 10^{-2}M$ HCl was used, and the etching time was of 1 minute and 2.5 minutes respectively. As expected the more concentrated acid was able to dissolve the window layers in a shorter time, with the CIGS layer being uniformly exposed after $45 - 60$ seconds.

In order to check for possible under-etching, the cross-section of the sample processed with the harshest etching conditions was analyzed through SEM imaging and compared with a section from the un-etched reference sample. The results are visible in figure 4.6. For the reference cell (figure 4.6a) the molybdenum, CIGS and top oxides layers are clearly visible.

In the picture of the cell that was processed through lithography (figure 4.6b) it is instead visible the step between the complete cell on the left, which was previously covered by the resist and therefore not etched, and the CIGS layer on the right, which was progressively exposed during the window layers removal. A low grade of under-etching is visible, with the step having a decreasing slope and going from maximum to minimum depth across a distance of $\sim 1\mu m$. This is however in-influential with respect to the total length of the subcells, which are at least 3 mm long. Since complete etching is obtained also for lower acid concentrations, the initial 10^{-2} is nevertheless maintained in the standard protocol.

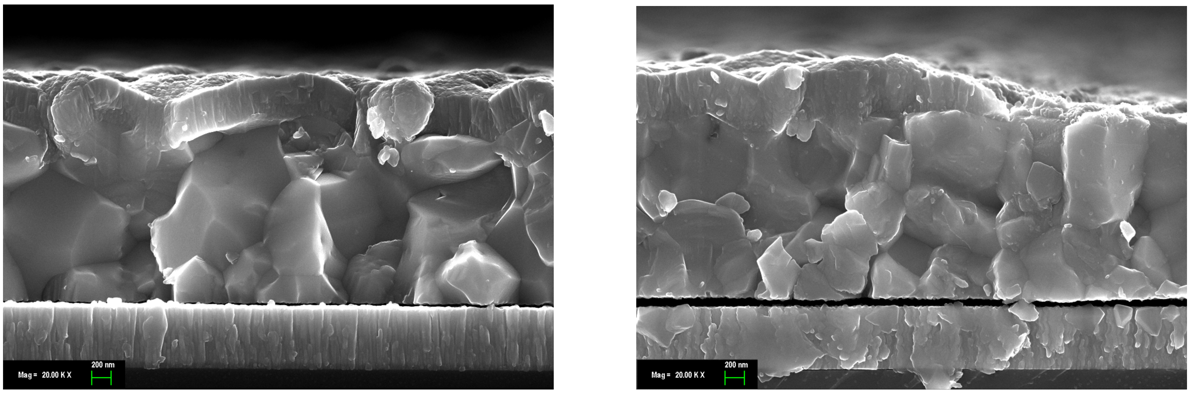

(a) SEM image of the section of the complete CIGS cell.

(b) SEM image of the section of a cell in correspondence of the step between the complete cell (left) and the area in which the window layers have been removed (right).

Figure 4.6: SEM image of the sections of differently processed CIGS cells.

Conclusions With the previous analysis it was shown that the etching of the window layer patterned through photolithography is an effective method for sub-cell division. Moreover the optimal etching time was found to be of 2.5 minutes when $10^{-2}M$ HCl is employed as the etchant solution. These parameters ensure sharp divisions between the areas and no oxide residues in the separation lines between subcells. Higher acid concentrations cause a low under-etching of the samples, and should therefore be avoided.

4.2 Validation of lithography process for grid deposition

In order to deposit the top contact grids through photolithography, additional steps have to be implemented. A first round of photolithography is necessary for grid deposition and a second for sub-cells division, as explained in detail in section 3.3.

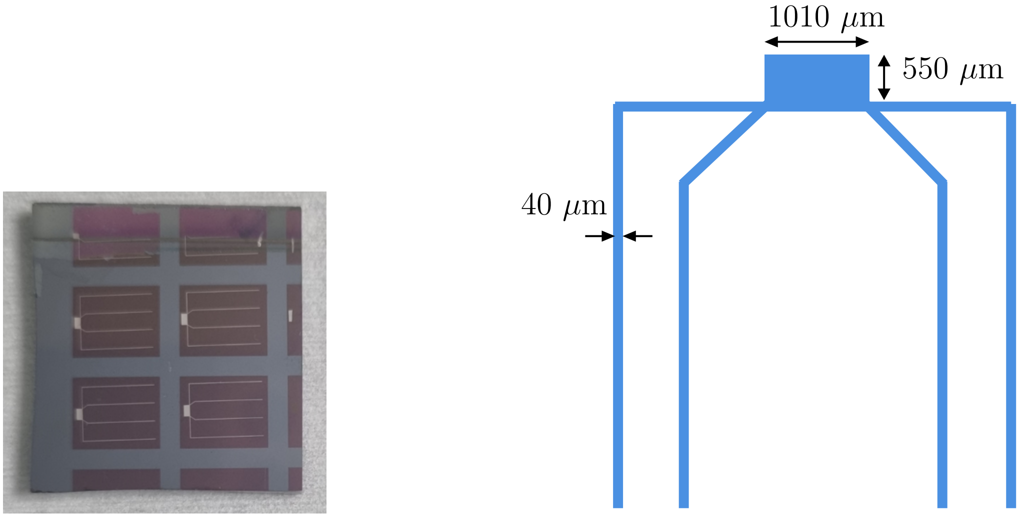

(a) Picture of a sample with both sub-cells and grids obtained through photolithography.

(b) Geometrical parameters of the grid obtained through profilometer measurements.

Figure 4.7: Geometrical features of the grids deposited through photolithography.

For this application the subcells are rectangular and have an area of $0.5\,cm^2$; each grid presents four fingers connected to a rectangular contact pad and is placed in the center of a sub-cell. A picture of the final device is visible in figure 4.7a.

The geometrical parameters of the grid mask were unknown, so they were measured through the analysis of their profiles. The profilometer was used to obtain the depth profiles across the fingers and contact pads, and the size of these features was determined by looking at the lateral position of the increases and decreases in depth. The values of finger width, pad width and pad length, obtained by averaging the measurements of two samples, are reported in figure 4.7b. The thickness of the deposited metal was too measured and it is equal to $710 \pm 10\,nm$, coherent with the expected thickness of $700nm$.

In order to check the correct morphology of the fingers pictures were taken, either through an optical microscope or through SEM, and are visible in figure 4.8. The finger edges appear straight and sharp, and there are no sections of the grids that appear to be peeling off of the oxides' surfaces.

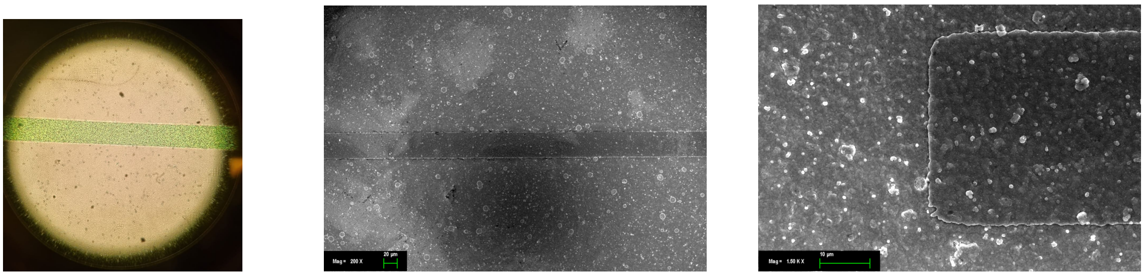

(a) optical microscope picture of a grid's finger, at 50× magnification.

(b) SEM picture of a grid's finger, at 200× magnification.

(c) SEM picture of the end of a grid's finger, at 1500× magnification.

Figure 4.8: grid's finger pictures

The scanning electron microscope was also employed to obtain cross section images of the device. Figure 4.9a shows the section in correspondence to a contact pad. The layer of evaporated metal is visible on top of the oxide surface. Figure 4.9b shows instead the section at the border between a finger (in the right side of the picture) and the surface of the complete cell (on the left side). It can be seen again how the edge of the finger is sharp and no under-etching is present.

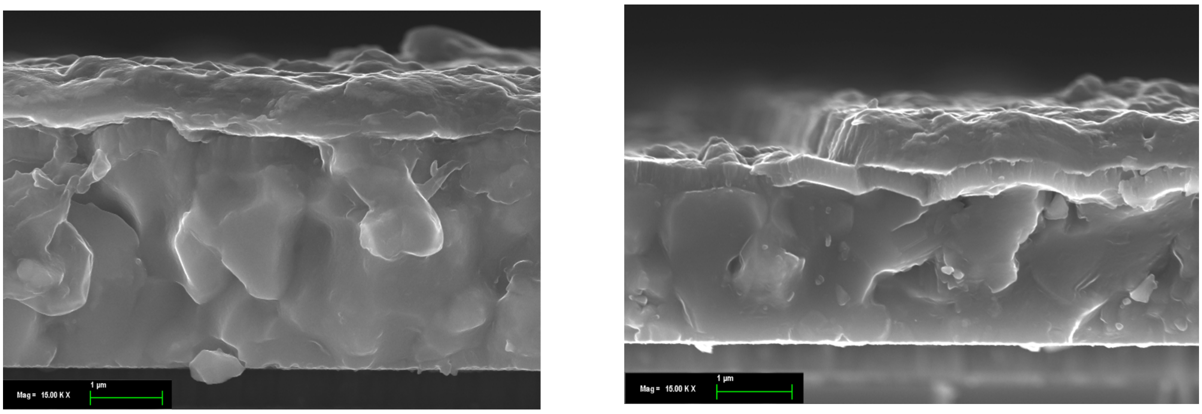

(a) SEM image of the cross-section of the cell in correspondence to a contact pad

(b) SEM image of the cross section of the cell at the edge of a finger.

Figure 4.9: SEM images of the cross sections of the cells with deposited metal grids.

Initially, the process for the application of the grids was performed in the opposite order: first the subcells were separated and only afterwards the pattern for the grids was created and the metal deposited. This, more intuitive, process led however to highly disuniform results, with many of the processed cells being completely unusable. Indeed the pattern for the grids in many cases did not develop properly so that parts or the fingers, or in same case the whole grid structure, peeled off from the surface during the resist lift-off. By observing the surface of the resist through an optical microscope, before grid deposition, it was possible to see how, when following this procedure (see figure 4.10a), the resist 'trenches' do not develop fully. This leads to the surface of the AZO layer being only partially exposed, as in the vertical line, or not exposed at all, as for the oblique line. This prevents the deposited metal from adhering to the cell's window layer and it is thus removed with the resist during the lift-off step.

This incomplete development was attributed to adhesion problems between the photomask and the cell during the grid exposure, caused by the fact that the surface of the cell divided in sub-cells is not at a uniform depth. Without the proper contact, the UV light is able to diffuse also under the mask, causing the final cross-link of parts of the resist that were supposed to remain soluble. As a result, during the development step only part of the resist is dissolved, reducing the expected width of the grids' features.

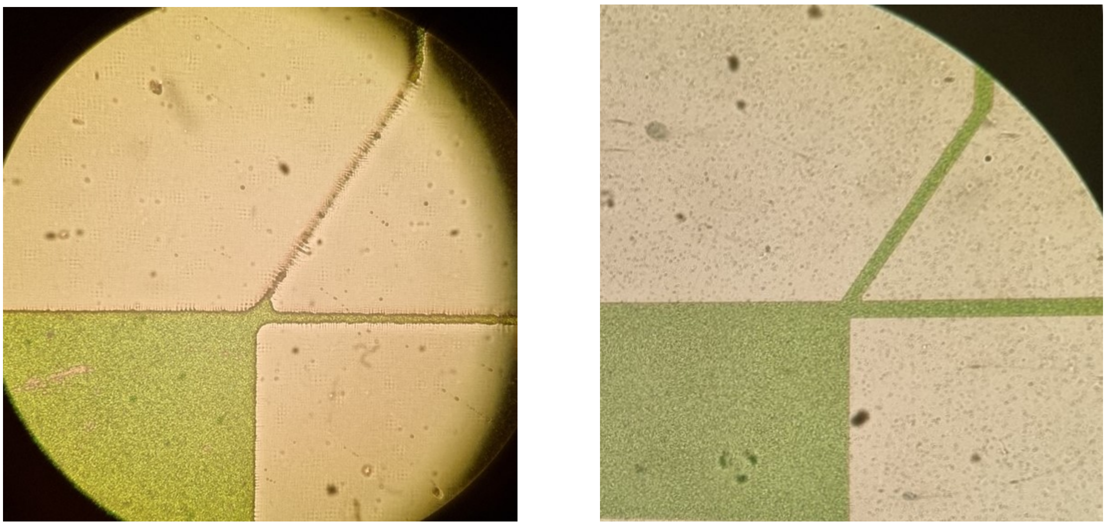

(a) Optical microscope image of the connection between a contact pad and the fingers in the case in which cell division was performed before finger deposition.

(b) Optical microscope image of the connection between a contact pad and the fingers in the case in which cell division was performed after finger deposition.

Figure 4.10: Optical microscope images of the patterned resist in correspondence to a grid's pad. The green areas correspond to the AZO layer, while the yellow, smooth surface is the photoresist.

By first depositing the grids and later dividing the sub-cells this problem is avoided, with the resist presenting sharp and uniform trenches, as visible in picture 4.10b. A SEM image of the cross section of the resist in this last case (see figure 4.11) proves its correct development. Moreover the negative slope of the photoresist, typical of image reversal resists, is also visible.

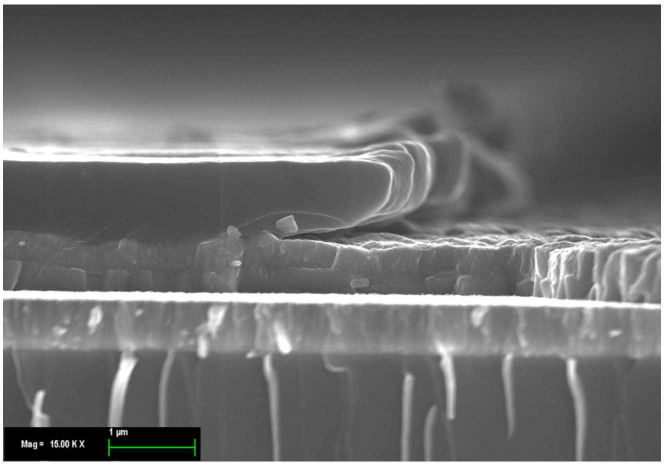

Figure 4.11: SEM cross section image of the edge of the developed photoresist, before grid deposition.

4.3 Opto-electronic characterization

It has been shown that the photolithography process is effective in selectively removing the window layers of the cell and the optimal parameters for the etching step have been determined. It is therefore necessary to test the opto-electronic property of the obtained device, in order to see if an improvement in performance with respect to the standard scribing method is indeed present.

To have a precise comparison each of the $2.5\,cm \times 2.5\,cm$ complete cells to be tested were cut in half. One side was processed through lithography, while the surface of the other half was scribed. Both halves are then subjected to I-V and EQE analysis, following the method explained in section 3.4.2. The results obtained with the two techniques are then compared.

Multiple tests were performed, on samples that differ for the area of the subcells, the energy gap, the buffer layer composition and the presence top contact grids. Results of the most relevant cases are reported in the following sections. Two standard sub-cell sizes are chosen. The smaller subcells are square and present an area of $0.09\,cm^2$ when scribed and an area of $0.10\,cm^2$ when they are obtained from the photomask. The bigger subcells are rectangular and they have an area of $0.5\,cm^2$ for both methods. In the case of scribing, the $0.5\,cm^2$ cells are completed with a top grid.

4.3.1 Characterization of small sub-cells

The most relevant case is the one for $0.10\,cm^2$ sub-cells processed by lithography, which are compared with $0.09\,cm^2$ sub-cells divided through scribing. The samples present the standard SLG/Mo/CIGS/ZnMgO/ZnOS/AZO structure, with standard CIGS energy gap of 1.18 eV. Three samples were analyzed, which differ for the power employed during the ZnMgO sputtering, that was of $70\,W$, $80\,W$ and $90\,W$ respectively.

A picture of the final appearance of the three samples, cut in half and divided in subcells, is visible in figure 4.12, where the cells on the top are the ones divided through photolithography while the cells on the bottom where divided through scribing.

Absorber characterisation First the CIGS absorber was characterized.

The composition profile of the CIGS layer has been analyzed through GDOES. As visible in figure 4.13, the CGI signal is mostly constant through the absorber, while the GGI increases with increasing depth. This trend is compatible with the energy gap grading strategy explained in section 2.1.2, with the front of the absorber presenting a lower gallium content than the back, and so a smaller energy gap, to enhance the separation of the generated charge carriers.

The XRF spectrum of the CIGS layer was also acquired. In table 4.4 are reported the concentrations of the element composing the absorber, in atomic concentration units.

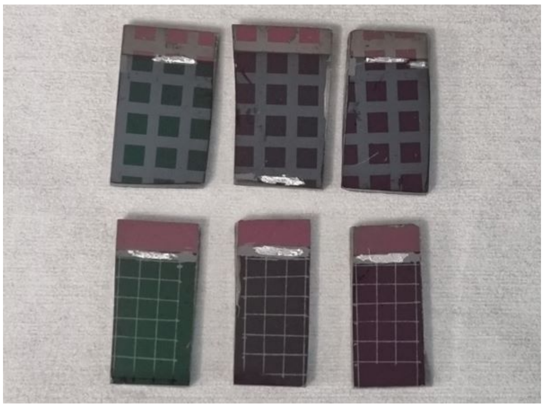

Figure 4.12: Picture of the three samples with small sub-cells, either divided by photolithography (on the top half of the picture) or by scribing (bottom half of the picture).

The GGI and CGI ratios are also indicated, and they are coherent with the values found through GDOES analysis.

Cu	In	Se	Ga	CGI	GGI
22.26	19.34	48.89	9.50	0.77	0.33

Table 4.4: Concentration of CIGS elements acquired by XRF spectroscopy and values of relative copper and gallium content.

The thickness of the CIGS layer and of the window layers were derived through profilometer measurements, respectively by looking at the step between Mo and CIGS and between the complete cell and the etched region. The results are reported in table 4.5. The thickness of the removed material is again in the 400-450 nm range, as it is expected for the previously deposited window layers, while the CIGS thickness is stable at around $2\mu m$.

Sample	CIGS (nm)	window layer (nm)
CIGS 70W	1990 ± 80	410 ± 10
CIGS 80W	2020 ± 60	480 ± 20
CIGS 90W	2030 ± 20	460 ± 10

Table 4.5: Thickness of CIGS layer and window layer determined with profilometer measurements.

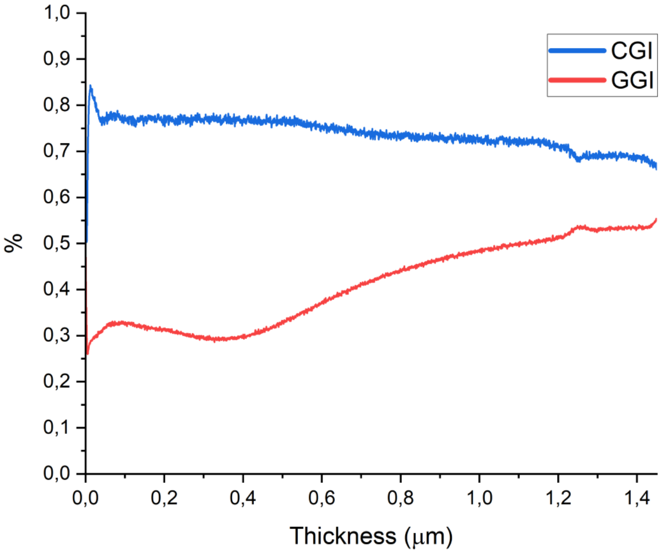

Figure 4.13: GDOES analysis of the CIGS absorber. The values of CGI and GGI ratios are visible as a function of the depth of the CIGS layer.

I-V characteristic A I-V measurement was performed on each sub-cell of the six resulting samples, following the procedure described in section 3.4.2. The scan was performed in both forward and reverse directions, from -0.1 V to 1.2 V, with a voltage step of 50 mV and a scan rate of 100 mV/s. By considering the area of the subcells, $0.09\,cm^2$ and $0.1\,cm^2$ for the scribing and lithography techniques respectively, it was possible to obtain the dependence on voltage of the cell's current density J.
Afterwards from these J-V curves the most relevant parameters characterizing the performance of the solar cells were calculated, namely the J_{sc}, the V_{oc}, the FF and the efficiency (η).

The most relevant information consists in the difference in performance between the two halves, the one with lithographed sub-cells and the one with scribed subcells, of each of three original samples (processed with sputtering at 70W, 80W and 90 W respectively). Indeed an improvement of these parameters was looked for in the cells processed through lithography.

In the box plots of figure 4.14 are reported the parameters distributions obtained from all the sub-cells of each sample; the mean value of each case is also specified and indicated with a small square. The variation between sub-cells of the same sample can be due to inhomogeneities in the absorber (as explained in section 4.1.2), but also due to mild damage during the window layers deposition and cell separation steps. In particular, subcells in proximity of the border of the cell often lead to non-uniform results, and are therefore removed from further analysis.

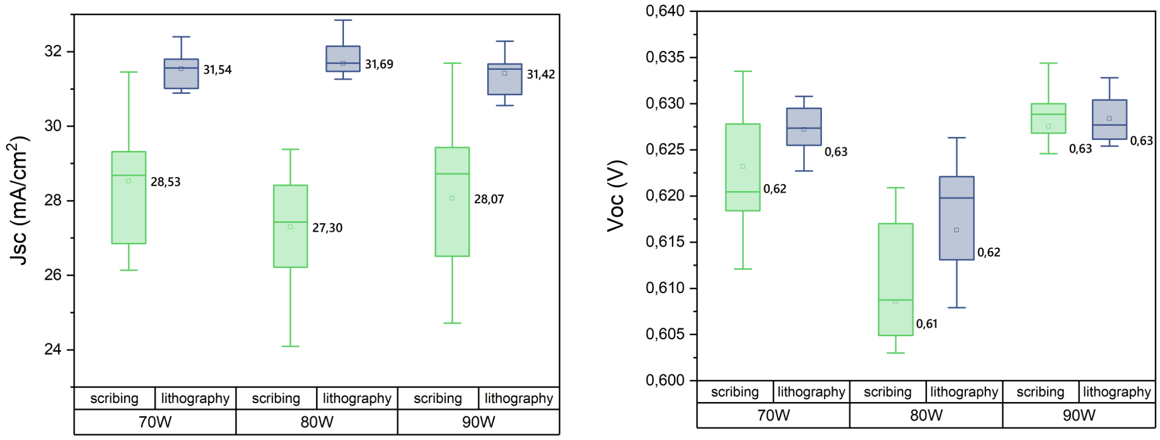

(a) J_{sc} (b) V_{oc}

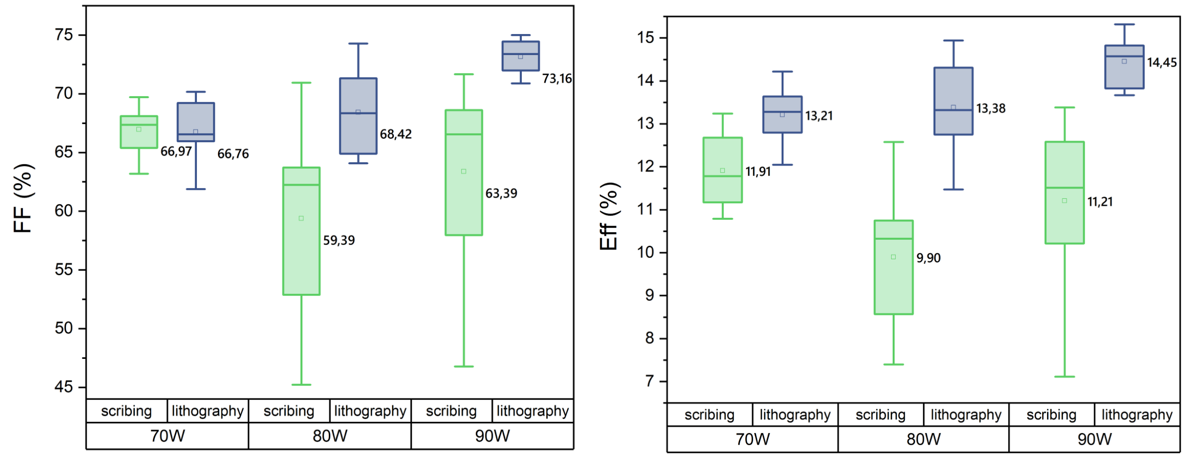

(c) FF (d) η

Figure 4.14: Box plots of the values of J_{sc}, V_{oc}, FF and efficiency η of the analyzed samples, divided by fabrication condition (70W, 80W, 90W) and sub-cell division technique (0.09 cm^2 subcells by scribing and 0.1 cm^2 subcells by lithography). The mean value of each distribution is also reported.

In figure 4.15 are instead visible the J-V characteristics of the sub-cells with the highest efficiency in each sample.

It can be seen that an improvement in the solar cells parameters is obtained by employing the lithography process. In particular (see figure 4.14a) there is a stark increase in the J_{sc} average values, which goes from 28 mA/cm^2 in the scribed cells to 31 mA/cm^2 in the lithographed cells ($\sim$ 10% increase). It can also be seen how, in the case of lithography, the distribution of values around the mean is much narrower than in the scribing case. This is favourable since it will lead to a more homogeneous behaviour of the device.

	70 W		80 W		90 W	
	Scribing	Lithography	Scribing	Lithography	Scribing	Lithography
Mean	11.9 ± 0.8	13.2 ± 0.7	10 ± 1	13 ± 1	11.2 ± 2	14.5 ± 0.6
Best	13.24	14.22	12.58	14.94	13.38	15.32

Table 4.6: Mean efficiencies and efficiency of best sub-cell in each analyzed sample.

On the other side no relevant difference has been observed in the case of the open circuit voltage (see figure 4.14b), with the values of V_{oc} being stable between 0.61 V and 0.63 V. A visible improvement has also been observed for two of the three initial samples in the fill factor value (figure 4.14c). Indeed for the cells processed at 80W and 90W there is a strong increase in the mean of the fill factor, reaching a 14% increase in the 90W case, and a decrease in the dispersion of values in the sides processed by lithography. No relevant changes were instead present for the 70W cell.

These results are reflected in the J-V characteristic shape. It can indeed be noted that the samples processed through lithography reach higher values of J_{sc} while keeping the same values of V_{oc} as the scribed samples. Moreover, it can be seen how the lithography curves reach a higher maximum power point, which entails a higher fill factor.

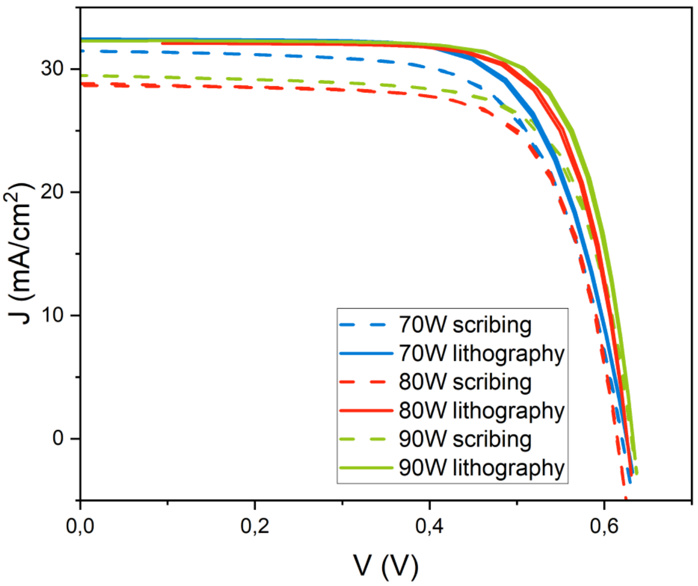

Figure 4.15: J-V characteristics of the best sub-cell in each sample.

All these factors lead to a consistent increase in efficiency for the cell processed by lithography. This is visible in table 4.6, in which the mean efficiencies calculated over all the subcells in each sample are visible, as well as the values of the best sub-cell efficiency for each sample.

EQE For the highest-efficiency subcells in each sample a EQE spectrum was also acquired (see section 3.4.2). The signal was collected for incident light with wavelengths between 300 nm and 1160 nm, with a 20 nm step. No relevant changes in the EQE shape and values were found between the two methods, especially for the 80W and 90W samples. This would imply that the encountered increase in J_{sc} is not dependent on the optical properties of the samples, so the lithography process improvement does not lay in the reduction of the sample's optical losses.

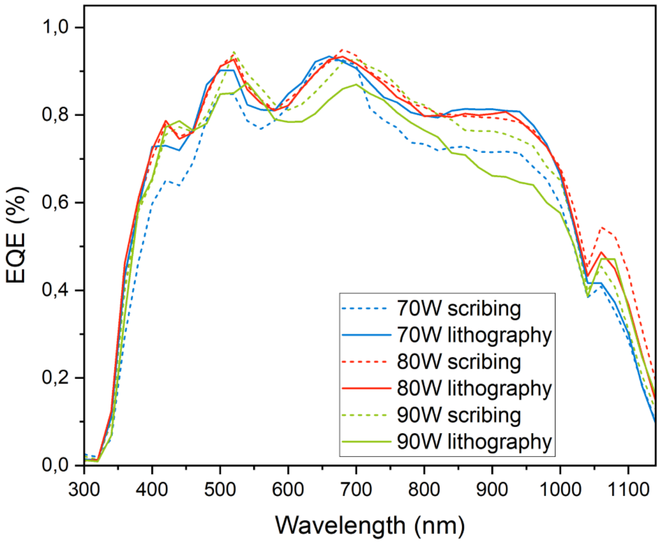

Figure 4.16: EQE spectrum of the best sub-cell in each sample.

Dark I-V characteristics Through the analysis of the EQE spectra it was possible to rule out the influence of optical factors in the increase of J_{sc}, and therefore of efficiency, for the cells processed through lithography. In order to better understand the origin of this variation, the I-V characteristic of the samples were acquired also in dark condition, following the process described in section 3.4.2. Indeed by fitting these curves with the two-diode model (see section 1.3) it's possible to obtain the values of the non-ideality factors n_1 and n_2, the saturation currents J_{01} and J_{01}, the series resistance R_{ser} and the shunt resistance R_{sh}. In particular from this model we would expect that higher values of saturation current J_0 lead to lower values of short circuit current J_{sc}. The series resistance instead impacts mostly the fill factor of the cells, with high R_{ser} leading to lower FF. Finally, high values of the shunt resistance determine higher values of J_{sc}, V_{oc} and FF.

The dark current parameters obtained by fitting the J-V curve of the sub-cells with the best efficiency in each sample are reported in table 4.7. It can be seen how the results follow quite closely the expected behaviour. The sides processed through lithography present a series resistance one order of magnitude lower than the scribing sides, which can explain the increase in fill factor previously found. Also the saturation currents present lower values in the case of lithography respect to scribing, justifying the observed increase in short circuit current. Finally the shunt resistances are higher for the lithography sides, thus leading to lower shunt current which in turn contributes to the higher values of J_{sc} and FF.

On the other side the fit doesn't return appropriate values for the non-ideality factors. Indeed for n_1 the expected value of $n_1 = 1$ is found and leads to good fitting curves, but on the other end the resulting values of n_2 are all higher than the expected maximum value $n_2 = 2$. To obtain more coherent results, a more complex fitting model could be considered, like the three diode model with resistance limited enhanced recombination [52]. In this case a third diode is added to the equivalent circuit, connected in parallel to the other two and coupled with a series resistance. This added diode takes in consideration the recombination current flowing through areas of increased resistance caused only by localized defects. This model can follow the cell behaviours not reproducible with the two diode model.

Sample		$J_{01}(A/cm^2)$	n_1	$J_{02}(A/cm^2)$	n_2	$R_{sh}(\Omega \cdot cm^2)$	$R_{ser}(\Omega \cdot cm^2)$
70 W	Scribing	1.64E-19	1 .01	7.29E-06	3.92	1.40E+03	221
	Lithography	5.10E-21	1.00	1.70E-07	5.42	5.78E+04	62
80 W	Scribing	7.53E-19	1.00	3.34E-06	2.86	9.96E+02	145
	Lithography	1.08E-21	0.99	5.27E-07	4.47	3.73E+04	11
90 W	Scribing	2.26E-19	1.02	7.92E-06	3.95	1.40E+03	224
	Lithography	7.34E-20	1.00	4.32E-08	3.65	4.53E+03	10

Table 4.7: Dark parameters values for the best sub-cell in each sample

Conclusions The cells processed through photolithography present a consistent improvement in efficiency, thanks to increased values of short circuit current and fill factor. In particular it is found that these improvement are determined by variations of the dark J-v characteristics parameters. Indeed sub-cells divided through lithography present lower values of R_{sh} and higher values of R_{ser} and J_0 compared to sub-cells divided by scribing, which in turn cause an increase in J_{sc} and FF. No variation in the external quantum efficiency is instead detected between the two processes. These observations lead to the conclusion that the selective nature of photolithography-based etching can prevent the formation of damaging cross-connections between the front and back contact, which can instead be present in cells processed through scribing. This in turn leads to an increase in free charge collection and sequentially in efficiency.

Therefore photolithography should be preferred as a method for sub-cells division for the fabrication of high-efficiency CIGS solar cells.

It is however relevant to note how this process is considerably more complex and more time consuming than simply scribing the surface of the cells. Moreover, it requires multiple steps and the usage of expensive chemicals and specialized equipment. As a reference, the processing of eight $2.5\,cm \times 2.5\,cm$ samples by a single operator at a lab scale can take up to three hours, compared to the few minutes necessary for scribing. Therefore in order to avoid the waste of time and resources a suggested procedure would be to first test a sample subdivided by scribing and then, in case of promising results, proceed with the lithography process on the remaining cells.

4.3.2 Characterization of wide band gap CIGS

Another relevant case is the one for wide band-gap CIGS, with $E_g = 1.62eV$. Indeed by increasing the band gap of CIGS it would be possible to employ this material as the top cell in a tandem configuration.

Four samples were considered, all coming from the same original cell with the structure SLG/Mo/CIGS/ZnOS/i-ZnO/AZO. The i-ZnO was deposited through ALD at varying temperature, namely 120°C, 140°C, 160°C and 180°C for the for samples. The complete cells were then divided in two parts. One was divided in $0.1\,cm^2$ sub-cells by lithography, while the other was divided in $0.5\,cm^2$ sub-cells by scribing. These bigger cells were then completed with Ni/Al/Ni top contact grids deposited by evaporation. The performances of the two kinds of cells were compared, in order to see if lithography is competitive also compared to cells with top grids and to find the achievable values of efficiency for wide band-gap solar cells.

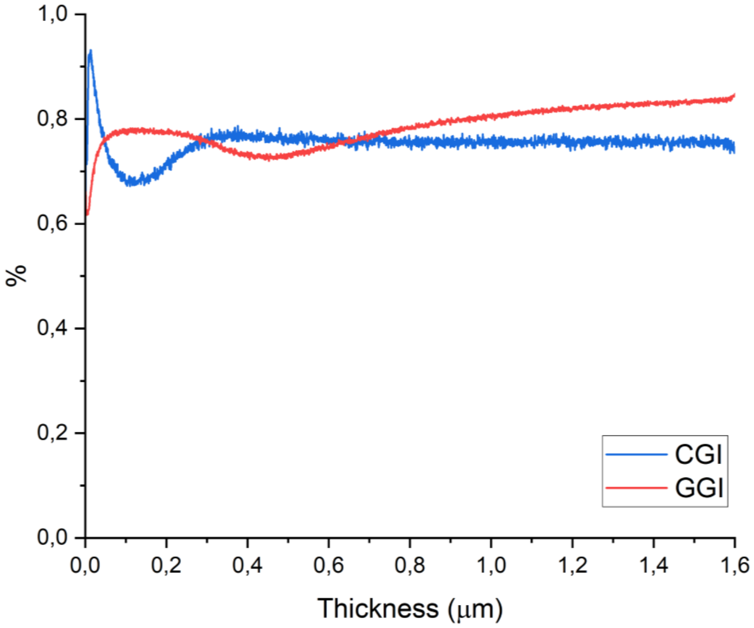

Figure 4.17: GDOES analysis of the CIGS absorber.

Absorber characterization The GDOES analysis results are visible in figure 4.17. The values of CGI is again fairly stable between 70% and 80%, while the GGI ratio is much higher than in the standard band-gap case, exceeding 80% in the bulk of the absorber. This is coherent with the fact that higher band-gaps are caused by higher gallium concentration. The same results for the gallium content are found from the XRF analysis of the sample (see table 4.8), in which a surface GGI of 76% is found. As a consequence the indium content of the layer is reduced, having a concentration of 6.70% compared to the 19.40% of the previous group of cells.

Cu	In	Se	Ga	CGI	GGI
20.24	6.70	53.03	20.04	0.76	0.75

Table 4.8: Concentration of CIGS elements acquired by XRF spectroscopy and values of relative copper and gallium content.

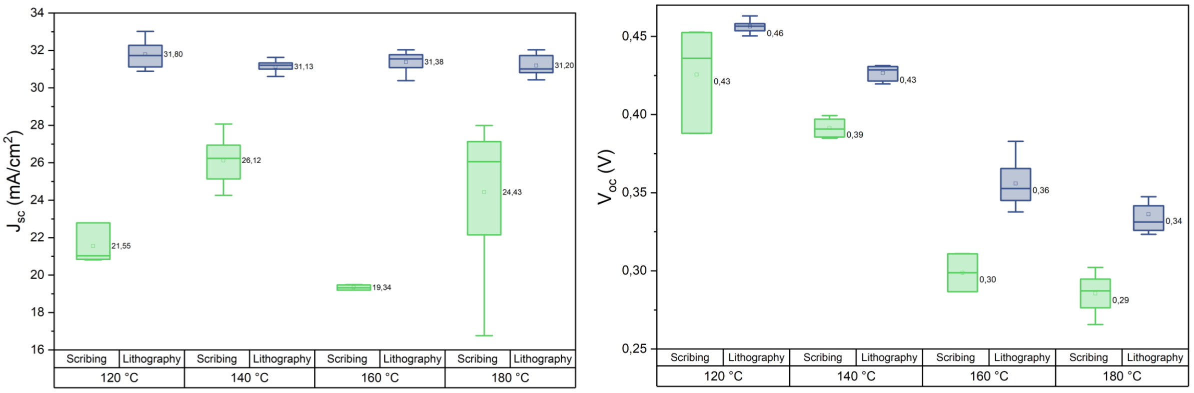

(a) J_{sc} (b) V_{oc}

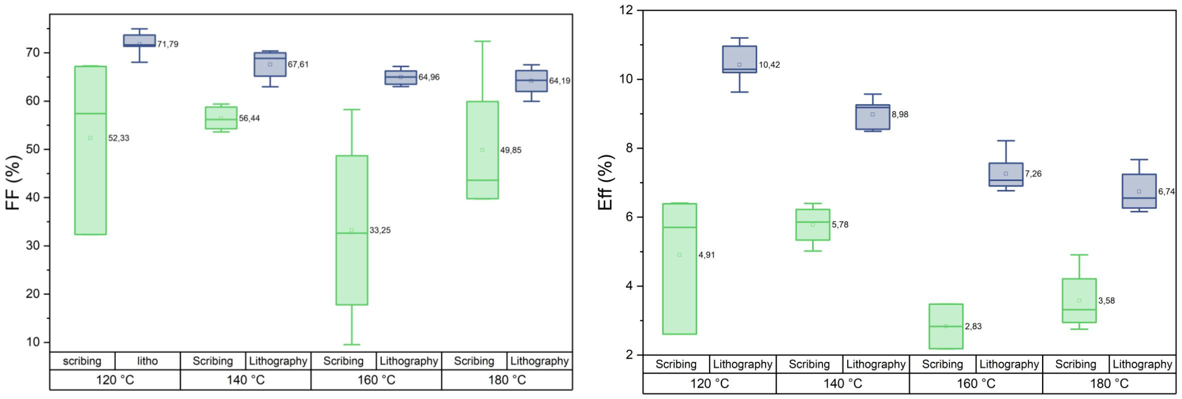

(c) FF (d) η

Figure 4.18: Box plots of the values of J_{sc}, V_{oc}, FF and efficiency η of the analyzed wide band-gap samples, divided by fabrication conditions (120°C, 140°C, 160°C, 180°C) and sub-cell division technique ($0.5\,cm^2$ subcells by scribing and $0.1\,cm^2$ subcells by lithography). In each case the mean value of the distribution is specified and marked by a square.

I-V characteristic For each sub-cell in the eight samples the J-V characteristic was acquired, considering a sample area of $0.5\,cm^2$ and $0.1\,cm^2$ for the scribing and lithography techniques respectively. From these curves the main solar cell parameters were obtained and are reported in figure 4.18.

For the cell processed through lithography there is, also in this case, a clear increase in the values of J_{sc}, with the best scribed sample having a average short circuit current of $26.12\,mA/cm^2$ and the relative lithographed half reaching $31.12\,mA/cm^2$. Regarding the open circuit voltage, a small increase, on average 13%, is found going from scribing to lithography. However the main dependence is on the ALD temperature, with the cells processed at 120°C having V_{oc} values which are 35% and 48% higher, for the scribed and lithographed cells respectively, than the values found for the cells processed at 180°C. The cells divided through lithography present also higher average values of fill factor than their scribed counterparts, meanwhile a clear dependence of FF on ALD temperature is not found. The resulting efficiency is influenced by these trends. Indeed it is found (see figure 4.18d and table 4.9) that the cells processed through lithography have a higher efficiency than the ones divided by scribing, with the sample processed at 120°C presenting an increase of 112% in the average efficiency between the two methods. Moreover, in the case of photolithography, samples with top layers deposited at a higher temperatures reach lower efficiencies than samples processed at lower temperatures.

	120°C		140°C		160°C		180°C	
	Scribing	Lithography	Scribing	Lithography	Scribing	Lithography	Scribing	Lithography
Mean	5 ± 2	10.4 ± 0.5	5.8 ± 0.5	9.0 ± 0.4	2.8 ± 0.7	7.3 ± 0.5	3.6 ± 0.9	6.7 ± 0.6
Best	6.41	11.20	6.40	9.57	3.48	8.22	4.91	7.67

Table 4.9: Mean efficiencies and efficiency of best sub-cell in each analyzed sample for the wide band-gap CIGS.

In figure 4.19 are reported the J-V characteristics of the best sub-cells of the different samples. It can be seen again how higher J_{sc} are reached by samples divided through lithography, which also have an higher maximum power point P_{max}. The dependence of the cells behaviour on the ALD temperature is also visible, with the sample processed at lower temperature giving better performance for both lithography and scribing.

Despite the improvements granted by the use of lithography, the maximum efficiency reached by wide band-gap solar cells are still lower than the ones for standard band-gap CIGS solar cells. Further optimizations of the cell structure are needed in order to make this technology competitive in the field of tandem solar cells.

EQE The EQE spectra for the best sub-cell in each sample was acquired, and the results are visible in figure 4.20. It can be noticed how for the sample processed at 120°C, 140°c and 180°C no differences in EQE shape and values are present between

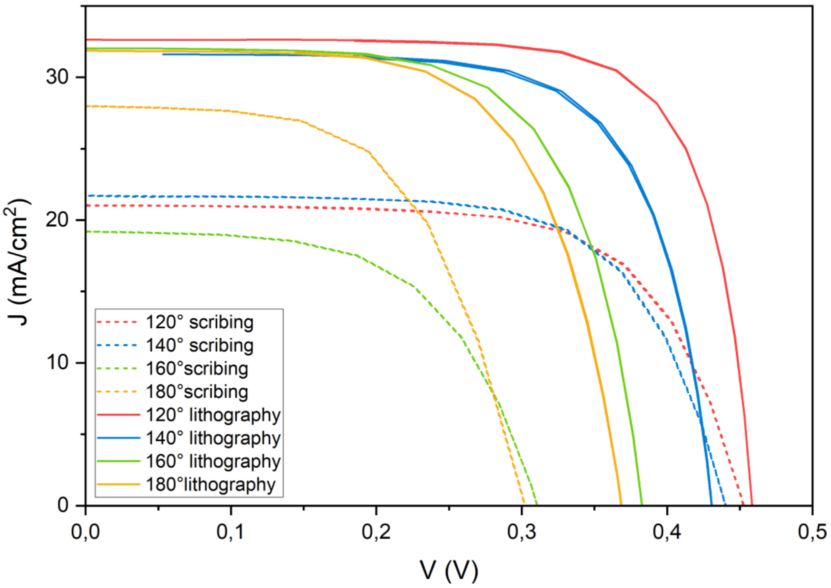

Figure 4.19: J-V characteristics of the best sub-cell in each sample.

sub-cells divided through lithography or through scribing. The values of EQE reached by the sample processed at 160°C and divided by scribing are substantially lower than the ones for all other samples. Since this sample presented also the worst J_{sc}, FF and efficiency, it is likely that the cell in question was damaged during the process or presented strong inhomogeneities. It was anyway excluded also in this case the the improvements observed in samples processed by lithography were caused by the reduction of optical losses.

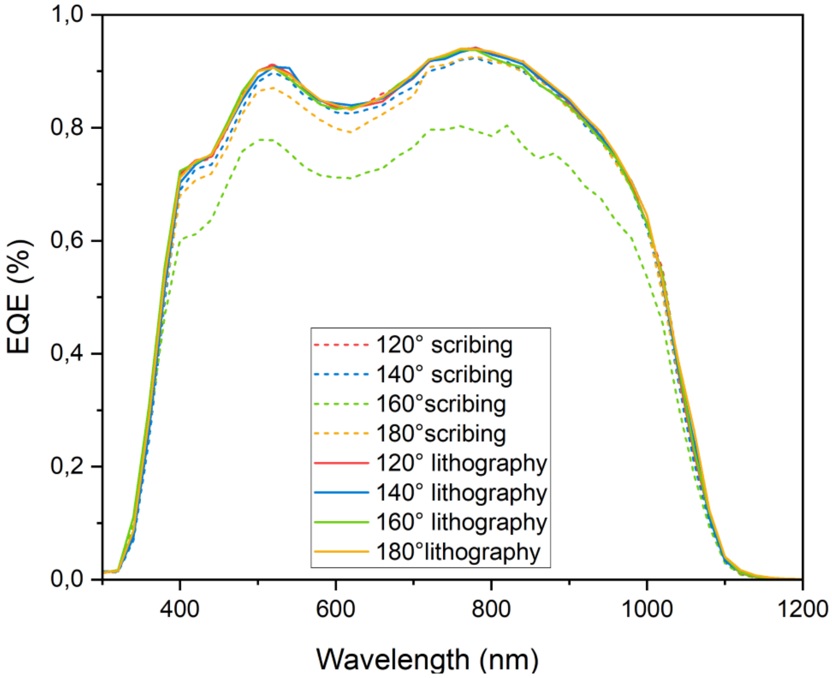

Figure 4.20: EQE spectrum of the best sub-cell in each sample.

4.3.3 Characterization of cells with top grids

The possibility of depositing top contact grids by photolithography was investigated. Three samples were considered, all originating from the same $10\,cm \times 10\,cm$ CIGS absorber and therefore presenting the identical structure: SLG/Mo/CIGS/ ZnOS/i-ZnO/AZO, with the i-ZnO deposited by ALD with a thickness of 50 nm. Top contact grids were deposited on a pattern created by photolithography and afterwards sub-cells were created also through photolithography. The subcells are rectangular, with an area of $0.5\,cm^2$, and the grids present the geometrical parameters shown in figure 4.7b. In the following the three samples will be indicated as $CIGS\_1$, $CIGS\_2$ and $CIGS\_3$.

A fourth identical sample was instead processed entirely without photolithography: the sub-cells were divided by scribing and the grids were created directly by metal evaporation through a mask. The sub-cells area is again $0.5\,cm^2$ while the grids present only two fingers. By comparing the performance of the cells processed with the two different methods it is possible to understand whether photolithography is a suitable method also for creating the pattern for the top grids.

Absorber characterization The GDOES results are reported in figure 4.21. It presents the classical behaviour for a standard band-gap CIGS, with a CGI ratio constant through the absorber and a GGI ratio that increases with increasing depth.

The values of concentrations of Cu, In, Ga and Se obtained through XRF spectroscopy are reported in table 4.10. The values of CGI and GGI at the surface are also shown. It can be seen that the value of CGI on the surface, 0.51%, is low compared to the one of the bulk, which can be deduced from the GDOES spectrum to be between 0.7% and 0.8%. This is compatible with the presence of the copper-poor ordered vacancy compound at the interface between CIGS and the buffer layer.

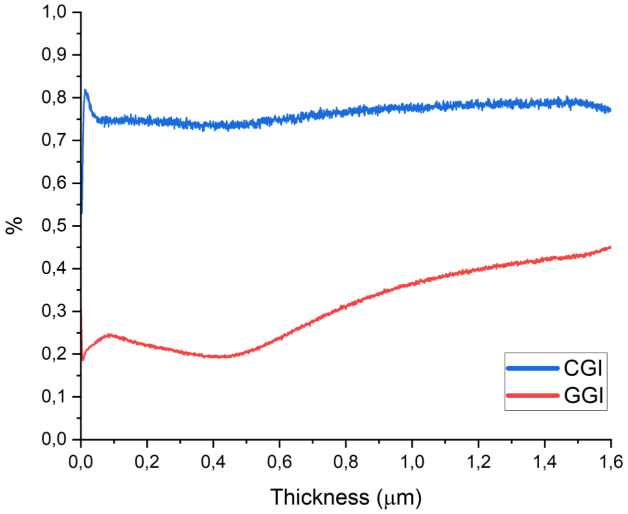

Figure 4.21: GDOES analysis of the CIGS absorber.

Cu	In	Se	Ga	CGI	GGI
17.64	25.98	47.54	8.74	0.51	0.25

Table 4.10: Concentration of CIGS elements acquired by XRF spectroscopy and values of relative copper and gallium content.

I-V characteristics For each sub-cell of the four samples a J-V characteristics was acquired and the values of short circuit current J_{sc}, open circuit voltage V_{oc}, fill factor FF and efficiency η were calculated. The results are visible in the box plots of figure 4.22.

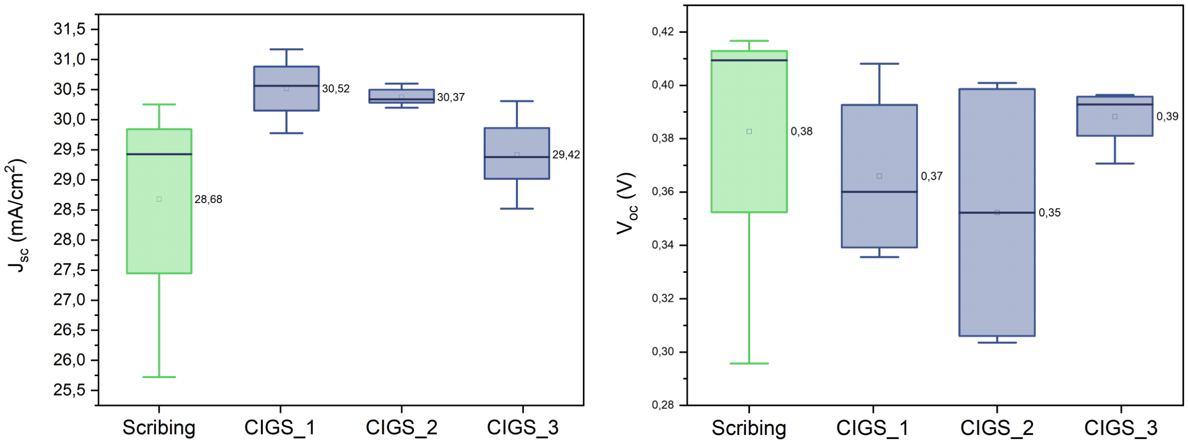

(a) J_sc (b) V_oc

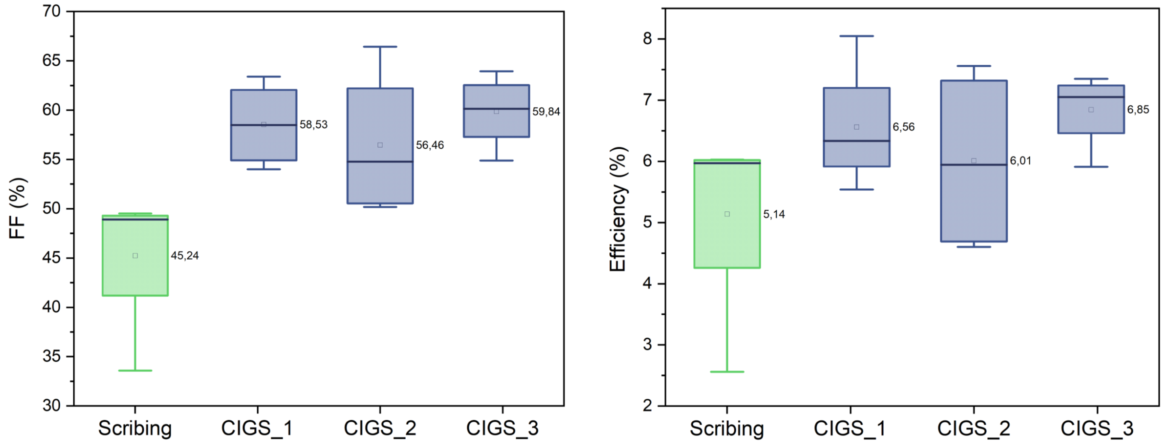

(c) FF (d) η

Figure 4.22: Box plots of the values of J_{sc}, V_{oc}, FF and efficiency η of the three samples processed through lithography and of the scribed sample. In each case the mean value of the distribution is specified and indicated by a square.

The cells processed through photolithography present higher average values of J_{sc} compared to the scribed cell and the dispersion between the subcells is much lower. No relevant changes in the open circuit voltage are instead registered between the two methods. On the other side there is a stark increase of the fill factor between the two sets of cell, with an average value of 58.28% among the cells processed by lithography compared to 45.24% for the scribing, with a total FF increment of 29%.

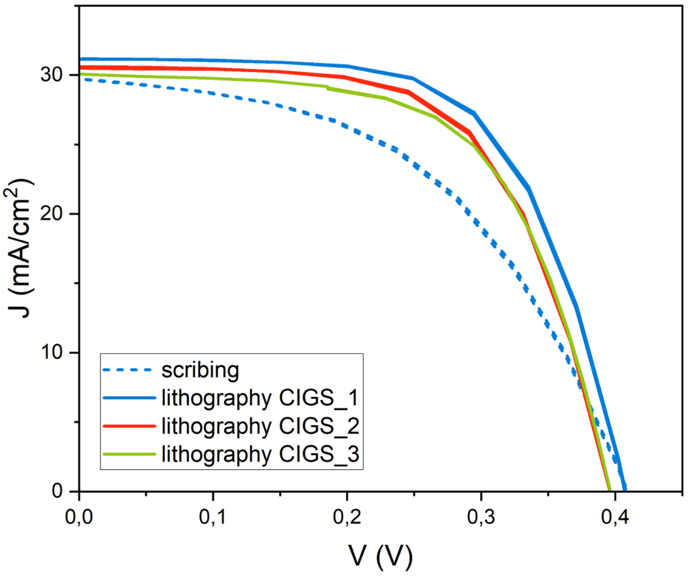

Figure 4.23: J-V characteristics of the best sub-cell in each sample for the three cells divided by lithography and the one divided by scribing. All cells are completed with top contact grids.

These trends are found again while comparing the J-V characteristics of the best subcells of the four samples (see figure 4.23): the cells processed through lithography present on average the same value of V_{oc} and a slightly higher value of J_{sc} with respect to the cell processed by scribing. The main difference lies in the maximum power point, and thus in the fill factor, of the curves, with the scribed cell presenting a P_{max} value strongly lower than the other samples do.

	Scribing	Lithograhy $CIGS\_1$	Lithograhy $CIGS\_2$	Lithograhy $CIGS\_3$
Mean	5 ± 1	6.6 ± 0.9	6 ± 1	6.8 ± 0.6
Best	6.03	8.05	7.56	7.35

Table 4.11: Mean efficiencies and efficiency of best sub-cell for every sample divided in $0.5\,cm^2$ sub-cells

These factors led to a net increase in efficiency for the photolithography cell, as can be seen in table 4.11 where the mean efficiency of each sample and the efficiency of the best sub-cell in the different samples are reported.

It is therefore found that photolithography can also be employed to create the patterns for the deposition of contact grids in wider area sub-cells, leading to final devices with higher efficiency than their scribed counterparts.

It is relevant to note that only four subcells were present for each sample, thus limiting strongly the statistics. In particular for the $CIGS\_2$ sample, the two subcells on one side of the sample presented values of V_{oc}, FF and efficiency greatly higher than the other two subcells, which leads to the wide dispersion of the obtained parameters. Being position-dependant, this variation is likely caused by inhomogeneities in the absorber.

Comparison with small cells The values of efficiency obtained for these wide-area subcells are much lower than the ones found for the $0.1\,cm^2$ subcells, described in section 4.3.1. This could be due to the different design of the subcells but also due to a lower quality of the initial complete cell. In order to understand the dependence of the efficiency on the cell quality, three more samples, taken from the same original cell, were analyzed. Two of those were divided in $0.1\,cm^2$ subcells through lithography and the remaining one in $0.09\,cm^2$ subcells through scribing. No grids were applied.

The resulting solar cell parameters and J-V curves are reported in figures 4.24 and 4.25. As for previous samples, also in this case an increase in J_{sc} and FF is visible for the lithographed samples, while no defined trend can be derived for the V_{oc}, leading to the assumption that its value is not dependent on the method used for cell division but mostly on the sample quality and homogeneity. From the J-V curves it is also visible how the maximum power point is remarkably higher in the cell processed through lithography, confirming the previous observations. This leads again to an increase of the cell efficiency (see table 4.12) with the lithography process leading to a 42% increase in efficiency when considering the best results for each sample.

	Scribing small cells	Litograhy $CIGS\_4$	Litograhy $CIGS\_5$
Mean	5 ± 1	9.6 ± 0.2	8.0 ± 0.5
Best	7.5	10.01	8.87

Table 4.12: Mean of efficiencies and efficiency of best sub-cell for every sample divided in small sub-cells.

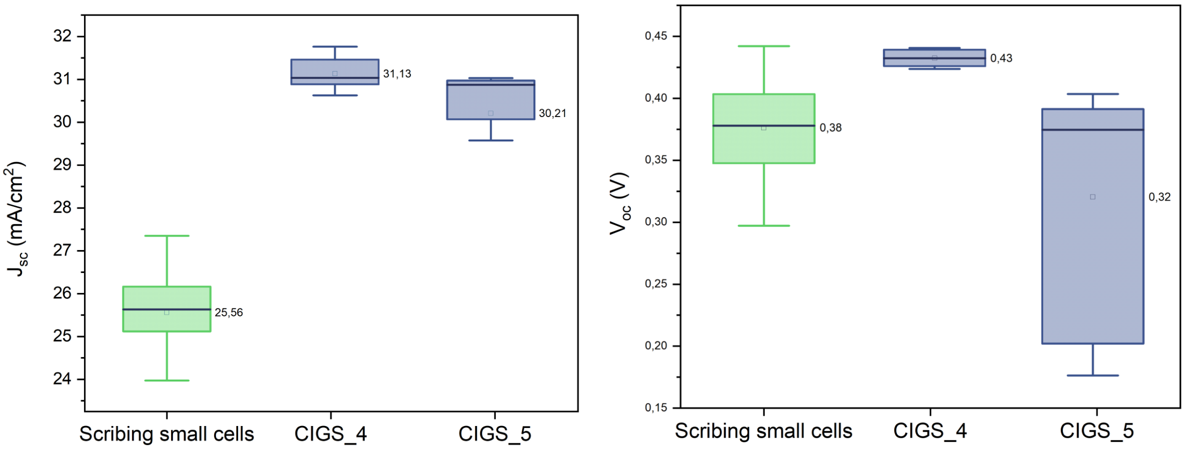

(a) J_{sc} (b) V_{oc}

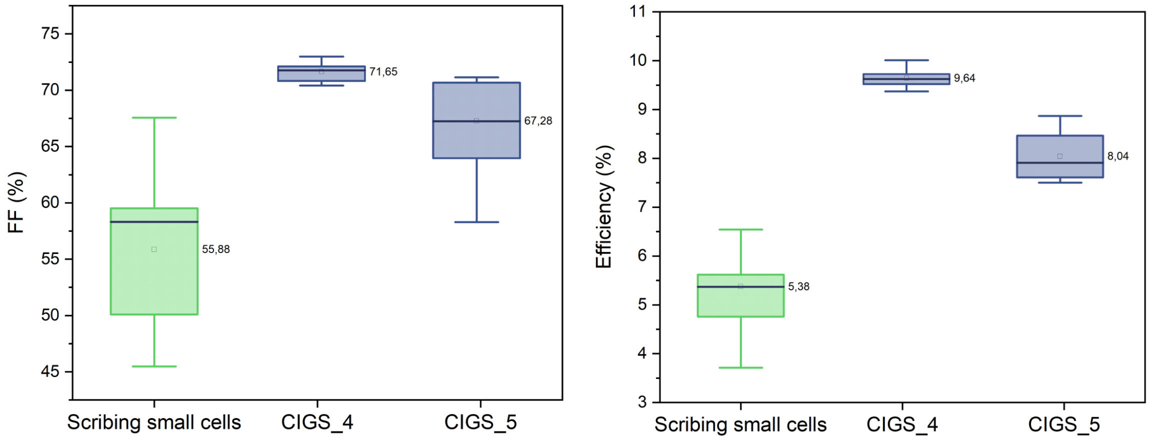

(c) FF (d) η

Figure 4.24: Box plots of the values of J_{sc}, V_{oc}, FF and efficiency η of the two samples processed through lithography and of the scribed sample. In each case the mean value of the distribution is specified and indicated by a square.

Comparing instead the results between the 0.1 cm^2 cells without grids and the 0.5 cm^2 with grids it's found that the smaller cells present a remarkably higher efficiency than the bigger cells. Indeed the average efficiency among the lithographed samples goes from 6.5% for the 0.5 cm^2 cells to 8.8% for the 0.1 cm^2 cells, so a total 36% increase.
These values are anyway still lower than the ones found in section 4.3.1, due to the difference in the deposition methods for the buffer layer. Indeed ZnMgO deposited by ALD is found to lead to lower performances in CIGS solar cells compared to deposition by sputtering.

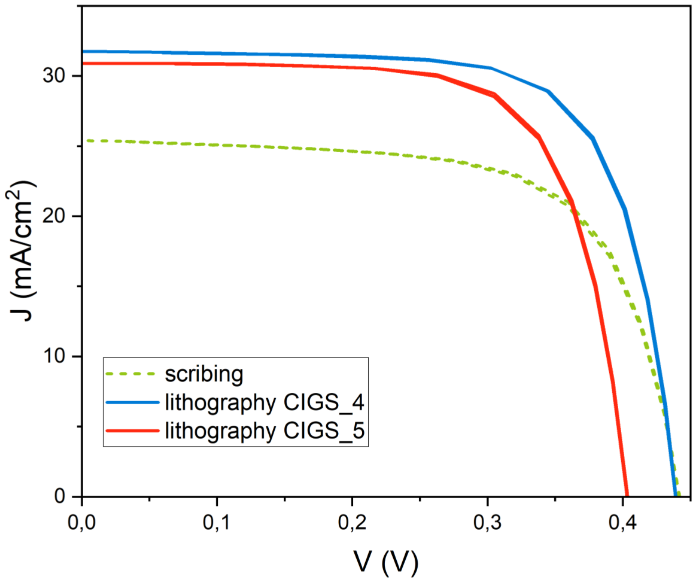

Figure 4.25: J-V characteristics of the best sub-cell in each sample for the two cells divided in 0.1 cm^2 sub-cells by lithography and the one divided in 0.09 cm^2 sub-cells by scribing.

EQE The EQE spectra of the best sub-cell in each of the four samples are reported in figure 4.26. It can be seen how also in the case of applied grids the values of EQE don't change significantly between the two methods, therefore ruling out optical factors in the increase of J_{sc}.

Dark I-V characteristics For the best sub-cells in the samples divided in 0.5 cm^2 sub-cells, the J-V characteristics in dark condition was acquired. This was done in order to better understand the improvement in efficiency, short circuit current and fill factor registered for the cells processed through lithography.

The parameters of $CIGS\_1$ and $CIGS\_2$ samples present the same trends, with respect to the scribed sample, found previously for the small subcells without grids.

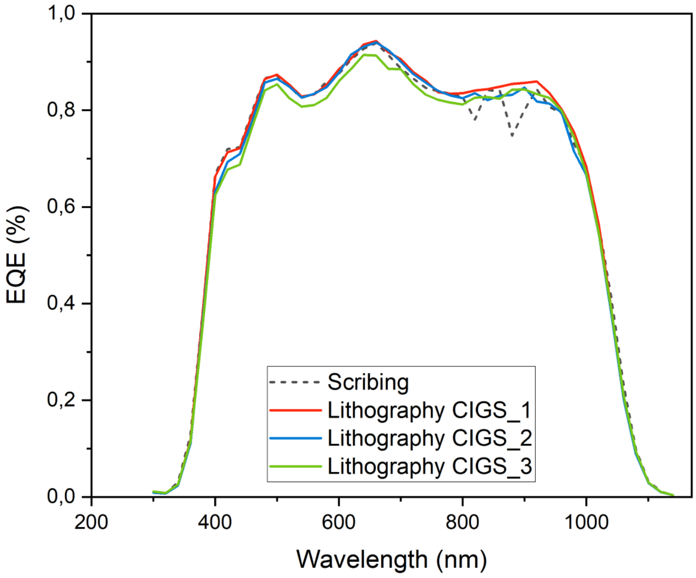

Figure 4.26: EQE spectra of the best sub-cell in each sample.

	$J_{01}(A/cm^2)$	n_1	$J_{02}(A/cm^2)$	n_2	$R_{sh}(\Omega \cdot cm^2)$	$R_{ser}(\Omega \cdot cm^2)$
Scribing	1.33E-12	0.99	8.28E-06	2.17	2.95E+02	2.1
CIGS_1	2.06E-12	1.48	2.48E-07	1.45	7.32E+03	1.07
CIGS_2	4.69E-12	1.58	7.51E-07	1.59	9.72E+03	1.01
CIGS_3	7.87E-11	1.54	1.04E-06	1.57	2.63E+02	1.47

Table 4.13: Dark parameters values for the best sub-cell with grids in each sample

Indeed J_{01} and J_{02} are lower in the case of lithography than in the case of scribing, which can explain the increase in J_{sc}. Similarly the obtained values of series resistance are half the values of the scribed cell, contributing to the improvement in fill factor. In these two cells processed through lithography moreover the shunt resistance is one order of magnitude higher than for the cell divided by scribing, ensuring higher values of FF and J_{sc}. All these effects can therefore lead to the better performance of the cells fabricated with the help of lithography.

In the case of the last lithographed sample, $CIGS\_3$, no visible difference is instead found with respect to the scribed sample. On the contrary some of its dark parameters would suggest poorer results in the illuminated J-V characteristics. Since the values in light conditions are averaged over different cells, it is possible that this unexpected result is caused by inaccuracies during the dark characteristic measurement.

Conclusions Samples with subcells divided through lithography, finished with top contact grids deposited again with the help of lithography, were analyzed and compared with samples divided through scribing and with grids deposited without the use of lithography. Better efficiencies were found for the cells processed with lithography than for the cells processed without, due to improvements in short circuit current and fill factor.

The obtained efficiencies were however much lower than the values found in previous tests for $0.1\,cm^2$ subcells. In order to understand if this downgrade was caused by the initial complete cells or by the grid deposition, more samples, originating from the same substrate, were divided in small subcells without grids and analyzed. The samples with the best performance were found to be the ones with $0.1\,cm^2$ sub-cells deposited by lithography, which presented however lower efficiencies than the ones found in previous analysis with the same top surface design.

Therefore from one side the quality of the initial cell was found to influence strongly the possible improvement obtainable by lithography, with the deposition of the window layer through sputtering giving better results. On the other side the smaller subcells lead to higher efficiencies respect to wider subcells with grids. Moreover the fabrication of the grids on a pattern created by lithography is a multi-step and time consuming process, since the resist deposition, exposure, development and liftoff steps need to be added to the metal evaporation. These factors make the division in smaller subcells with no added grids the design with the better trade-off between time consumed and improvement in cell performance.

Since wider area subcells are however favoured for the industrialization of the process and for the integration of the cells in modules, a viable alternative could be the division of the samples in $0.5\,cm^2$ sub-cells by photolithography, and then the deposition of the top contact grids directly by evaporation through a patterned mask. This design would combine the efficiency improvement of lithography with an easier and faster fabrication process.

Conclusions

In this work, a sub-cell division method based on photolithography was successfully applied to CIGS solar cells.

The process, based on the etching of the buffer and top contact layers through a photoresist pattern created by photolithography, has been tested on different architectures of CIGS cells, and has been proven to be effective in selectively removing these top layers while leaving the absorber undamaged. This technique additionally exhibits far greater geometrical resolution with respect to mechanical scribing, and ensures the presence of sharp division lines. This represents an improvement in comparison to the jagged separation lines typically obtained through the scribing method.

The photolithography and etching parameters have been optimized to guarantee a complete and clean removal of the desired sections. The final morphology of the cells has been analyzed through scanning-electron microscope imaging and profilometry scans to examine the thickness of the obtained layers and the geometrical features of the divided subcells. X-ray fluorescence spectroscopy and glow discharge optical emission spectroscopy analyses were performed to acquire the absorber's elemental composition and ensure that no modifications took place after the photolithography and etching procedure. These techniques also confirmed the complete removal of the zinc-based top layers.

Successively the opto-electronic performance of the sub-cells divided through photolithography has been tested. The J-V characteristics of the subcells, in both dark and illuminated conditions, have been acquired and compared to analogous measurements performed on samples divided into sub-cells through scribing. A consistent increase in the cell's efficiency has been recorded in samples divided by lithography, owing to improvements in the cells' short circuit current and fill factor. No conclusive variations in the value of the open circuit voltage were instead recorded. An average increase in efficiency of 30% between the two methods was obtained for standard (1.18 eV) band-gap CIGS. Analogous positive results were obtained for cells based on wide band-gap CIGS (1.62 eV), for which the average efficiency improvement reached levels of up to 80%. It has to be noted that in this case the tested sub-cells presented a different surface area, which may have had an impact on the results.

External quantum efficiency analyses were performed for cells processed with the two methods. No significant variations were found in the obtained spectra, resulting in the exclusion of optical phenomena from the possible factors which lead to performance improvement in samples processed by lithography. In contrast, the analysis of the current density-voltage curves in dark conditions showed an increase in shunt resistance and a decrease in series resistance and saturation currents for samples divided by lithography, which can explain the increase in short circuit current and fill factor obtained in the illuminated case.

It was therefore found that photolithography-based cell division, through the selective etching of only the buffer and top contact layers, was able to increase the efficiency of the final cell. This outcome is due to the elimination of cross-connections between the back and the front contacts, which ensures a higher charge carrier collection. This particular result is encouraging with regards to applications in tandem solar cells employing CIGS as the top cell, since it makes it possible to effectively divide the sub-cells without causing damage on any of the underlying layers.

Photolithography was also employed to create a pattern for the deposition of top metallic grids, which are typically used to enhance charge collection in wider area sub-cells. Sample presenting top grids deposited through photolithography and divided into sub-cells again with the help of lithography were fabricated. Their performance was then compared to the one of cells with grids processed completely without the use of lithography. Again, an increase in short circuit current and fill factor, which led to an increase in efficiency, was observed for the first method. However, both samples with grids had worse performance than analogous samples divided in smaller cells without grids. This suggests that the improvement is mostly related to the cell division process and not to the grid deposition method. Moreover, grid deposition through photolithography is a multi-step and time-consuming process, which decreases the possibility of application in larger-scale fabrication.

Therefore a mixed configuration presenting sub-cells divided through photolithography and grids deposited through direct evaporation is suggested. More tests need to be performed to verify the opto-electronic performance of this design and to reduce the fabrication time, in the perspective of industrialization of production.

Acknowledgements

I would first like to thank Professor Daniela Cavalcoli at the University of Bologna, who guided me in the preparation of this master thesis. I also want to thank Dr. Negar Naghavi and Dr. Jackson Lontchi who supervised me during the experimental work at the Institute Photovoltaique de l'Ile de France and who made this work possible. I'm also really thankful to Amelle Rebai and Alexandre Py for the support and the help they provided in the laboratory.

Bibliography

[1] Simon Philipps, Fraunhofer Ise, Werner Warmuth, and Pse Projects GmbH. Photovoltaics report, 2023.

[2] REN21. Renewables 2023 global status repor, 2023.

[3] Martin A. Green, Ewan D. Dunlop, Masahiro Yoshita, Nikos Kopidakis, Karsten Bothe, Gerald Siefer, and Xiaojing Hao. Solar cell efficiency tables (version 63). *Progress in Photovoltaics: Research and Applications*, 32(1):3–13, 2024.

[4] Shogo Ishizuka, Yukiko Kamikawa, and Jiro Nishinaga. Lightweight and flexible cu(in,ga)se2 solar minimodules: toward 20 *npj Flexible Electronics*, 6, 12 2022.

[5] J. Nelson. *The Physics of Solar Cells*. Series on Properties of Semiconductor Materials. Imperial College Press, 2003.

[6] Louis Gouillart. Development of ultrathin cu(in,ga)se2-based solar cells with reflective back contacts.

[7] Peter Würfel. *Physics of Solar Cells: From Principles to New Concepts*. 2007.

[8] Yuan Zhao, Ming-Yu Sheng, Wei-Xi Zhou, Yan Shen, Hu Ertao, Jian-Bo Chen, Yu-Xiang Zheng, Youngpak Lee, D. Lynch, and Liang-Yao Chen. A solar photovoltaic system with ideal efficiency close to the theoretical limit. *Optics express*, 20:A28–38, 01 2012.

[9] Daniel Abou-Ras, Thomas Kirchartz, Uwe Rau, and Wiley-VCH. *Advanced Characterization Techniques for Thin Film Solar Cells*.

[10] William Shockley and Hans J. Queisser. Detailed Balance Limit of Efficiency of p-n Junction Solar Cells. *Journal of Applied Physics*, 32(3):510–519, 03 1961.

[11] Jean-Francois Guillemoles, Thomas Kirchartz, David Cahen, and Uwe Rau. Guide for the perplexed to the shockley-queisser model for solar cells guide for the perplexed to the shockley-queisser model for solar cells solar energy conversion and the shockley-queisser model, a guide for the perplexed. *Nature Photonics*, 13, 2019.

[12] Ehsan Raza and Zubair Ahmad. Review on two-terminal and four-terminal crystalline-silicon/perovskite tandem solar cells; progress, challenges, and future perspectives. *Energy Reports*, 8:5820–5851, 2022.

[13] Miguel Anaya, Gabriel Lozano, Mauricio E. Calvo, and Hernán Míguez. Abx3 perovskites for tandem solar cells, 12 2017.

[14] Antonino Parisi, Riccardo Pernice, Vincenzo Rocca, Luciano Curcio, Salvatore Stivala, Alfonso C. Cino, Giovanni Cipriani, Vincenzo Di Dio, Giuseppe Ricco Galluzzo, Rosario Miceli, and Alessandro C. Busacca. Graded carrier concentration absorber profile for high efficiency cigs solar cells. *International Journal of Photoenergy*, 2015, 2015.

[15] M. J. De Wild-Scholten. Energy payback time and carbon footprint of commercial photovoltaic systems. *Solar Energy Materials and Solar Cells*, 119, 2013.

[16] Davide Polverini, Nieves Espinosa, Umberto Eynard, Enrica Leccisi, Fulvio Ardente, and Fabrice Mathieux. Assessing the carbon footprint of photovoltaic modules through the eu ecodesign directive. *Solar Energy*, 257, 2023.

[17] Marianna Kemell, Mikko Ritala, and Markku Leskelä. Thin film deposition methods for cuinse2 solar cells. *Critical Reviews in Solid State and Materials Sciences*, 30:1–31, 03 2005.

[18] Fabien Mollica, Marie Jubault, Frederique Donsanti, Anaïs Loubat, Muriel Bouttemy, Arnaud Etcheberry, and Negar Naghavi. Light absorption enhancement in ultra-thin cu(in,ga)se2 solar cells by substituting the back-contact with a transparent conducting oxide based reflector. *Thin Solid Films*, 633, 2017.

[19] Louis Gouillart, Andrea Cattoni, Wei Chao Chen, Julie Goffard, Lars Riekehr, Jan Keller, Marie Jubault, Negar Naghavi, Marika Edoff, and Stéphane Collin. Interface engineering of ultrathin cu(in,ga)se2 solar cells on reflective back contacts. *Progress in Photovoltaics: Research and Applications*, 29, 2021.

[20] Rebekah L. Garris, Jian V. Li, Miguel A. Contreras, Kannan Ramanathan, Lorelle M. Mansfield, Brian Egaas, and Ana Kanevce. Efficient and stable cigs solar cells with znos buffer layer. 2014.

[21] Motoshi Nakamura, Koji Yamaguchi, Yoshinori Kimoto, Yusuke Yasaki, Takuya Kato, and Hiroki Sugimoto. Cd-free cu(in,ga)(se,s)2 thin-film solar cell with record efficiency of 23.35*IEEE Journal of Photovoltaics*, 9(6):1863–1867, 2019.

[22] D. Hariskos, B. Fuchs, R. Menner, N. Naghavi, C. Hubert, D. Lincot, and M. Powalla. The zn(s,o,oh)/znmgo buffer in thin-film cu(in,ga)(se,s)2-based solar cells part ii: Magnetron sputtering of the znmgo buffer layer for in-line coevaporated cu(in,ga)se2 solar cells. *Progress in Photovoltaics: Research and Applications*, 17:479–488, 11 2009.

[23] Billel Salhi. The photovoltaic cell based on cigs: Principles and technologies, 3 2022.

[24] Archer Mary and Green Martin. *CLEAN ELECTRICITY FROM PHOTOVOLTAICS 2nd Edition*, volume 4. 4th edition, 2015.

[25] M. I. Alonso, M. Garriga, C. A. Durante Rincón, E. Hernández, and M. León. Optical functions of chalcopyrite cugaxin1-xse2 alloys. *Applied Physics A: Materials Science and Processing*, 74:659–664, 5 2002.

[26] P. M.P. Salomé, H. Rodriguez-Alvarez, and S. Sadewasser. Incorporation of alkali metals in chalcogenide solar cells, 7 2015.

[27] Xinxing Liu, Junjun Zhang, Liting Tang, Junbo Gong, Wang Li, Zengyang Ma, Zexin Tu, Yanyan Li, Ruiming Li, Xuzhi Hu, Chen Shen, He Wang, Zhiping Wang, Qianqian Lin, Guojia Fang, Sheng Wang, Chang Liu, Zengming Zhang, Jianmin Li, and Xudong Xiao. Over 28*Energy and Environmental Science*, 16:5029–5042, 6 2023.

[28] Nicolas Barreau, Olivier Durand, Eugène Bertin, Antoine Létoublon, Charles Cornet, Polyxeni Tsoulka, Eric Gautron, and Daniel Lincot. Epitaxial growth of cigse layers on gap/si(001) pseudo-substrate for tandem cigse/si solar cells. *Solar Energy Materials and Solar Cells*, 233, 12 2021.

[29] Thomas Adams and Richard Layton. *Introductory MEMS: Fabrication and Applications*. 01 2010.

[30] Chris A. Mack. *Fundamental principles of optical lithography : the science of microfabrication*. Wiley, 2007.

[31] T.J. Rinke, C. Koch, and MicroChemicals GmbH. *Photolithography: Basics of Microstructuring*. MicroChemicals, 2017.

[32] F. Pommereau, M. Iost, F. Vollenbroek, and S. Gourrier. Resist profile control of image reversal process in contact lithography. *Microelectronic Engineering*, 9(1):591–594, 1989.

[33] Roberto Mosca and Marco Calicchio. Technological processes for cigs based solar cells.

[34] Joop van Deelen and Corné Frijters. Cigs cells with metallized front contact: Longer cells and higher efficiency. *Solar Energy*, 143, 2017.

[35] Paolo A Losio, Thomas Feurer, and Stephan Buecheler. Evolutionary optimization of tco/mesh electrical contacts in cigs solar cells.

[36] Joop Van Deelen, Corné Frijters, Matthijs Suijlen, and Marco Barink. Influence of the grid and cell design on the power output of thin film cu(inga)se2 cells. *Thin Solid Films*, 594, 2015.

[37] Helmut Fischer Group. Fischerscope® x-ray xdv®-sdd.

[38] Michael Haschke, Jörg Flock, and Michael Haller. *X-ray Fluorescence Spectroscopy for Laboratory Applications.* 2021.

[39] Bharat Bhushan. *Modern Tribology Handbook, Two Volume Set.* 2000.

[40] Nicholas X. Randall. *Experimental methods in tribology*, volume 9781461419457. 2013.

[41] Patrick Chapon, Sofia Gaiaschi, and Kenichi Shimizu. *Glow Discharge Optical Emission Spectrometry*, pages 219–228. Springer Singapore, Singapore, 2018.

[42] Horiba. Gd-profiler 2tm pulsed rf glow discharge optical emission spectrometer with differential interferometry profiling, 2020.

[43] Yasuyuki Okano. *Scanning Electron Microscopy*, pages 563–569. Springer Singapore, Singapore, 2018.

[44] Merck Performance Materials GmbH. *AZ 5214 E Photoresist Technical Data Sheet.*

[45] SÜSS MicroTec. Ma6 / ma8 manual mask aligner.

[46] Horiba. https://www.bruker.com/en/products-and-solutions/test-and-measurement/stylus-profilometers/dektakxt.html, 2020.

[47] Carl Zeiss Microscopy GmbH. Merlin series brouchure.

[48] Oriel instruments. Class aaa solar simulators datasheet, 2019.

[49] Cicci research. Arkeo an all-in-one measurement platform.

[50] Suncheul Kim, Chang Soo Lee, Seungtae Kim, R. B.V. Chalapathy, Essam A. Al-Ammar, and Byung Tae Ahn. Understanding the light soaking effect of znmgo buffer in cigs solar cells. *Physical Chemistry Chemical Physics*, 17, 2015.

[51] BioLogic. Sp-150 potentiostat.

[52] Keith McIntosh. *Lumps, Humps and Bumps: Three Detrimental Effects in the Current–Voltage Curve of Silicon Solar Cells.* PhD thesis, University of New South Wales, 01 2001.